Electrochemical modeling of single particle intercalation battery materials with different thermodynamics

Wei Lai*

Department of Chemical Engineering and Materials Science, Michigan State University, East Lansing, MI 48824, USA

ARTICLE INFO

ABSTRACT

Current–voltage relations of a single intercalation battery electrode particle were modeled with the step current, step voltage, linear sweep voltage, and sinusoidal current signals. A solid solution with constant diffusivity, a solid solution with variable diffusivity, and a phase transformation material were considered for their thermodynamic and kinetic evaluations based on the regular solution model and the generalized Poisson–Nernst–Planck equations. The numerical simulation results were compared with known, small-signal solutions and experimental data throughout the article.

© 2011 Elsevier B.V. All rights reserved.

1. Introduction

Electrode particles in intercalation batteries work by the insertion/intercalation and extraction/deintercalation of ions and electrons to and from the host. In the case of lithium intercalation, lithium ions enter the interstitial polyhedral sites while electrons bind to the transition metal sites as polarons or band electrons. Not only lithium ions and electrons occupy different sites in the host, they also come from different external sources, e.g. electrolyte for lithium ions and current collector for electrons.

The ambipolar charge transport of ions and electrons can be modeled by the Poisson–Nernst–Planck (PNP) equations composed of the Nernst–Planck, continuity equations, and Poisson equation. The PNP equations have been widely used in liquid electrochemistry, semiconductors, and ionic channels in biological membranes [1–4], among others. Another popular view of lithium ion and electron insertion is to treat it as the equivalent of the insertion of a neutral lithium species, which has been modeled by Fick's laws [5]. Both the classical PNP equations and Fick's laws are partial differential equations that track concentrations and mass fluxes. This makes them inconvenient for electrochemical modeling, which typically concerns the current–voltage relationship. Classical PNP equations can be reformulated as equations, that involve current (density) and voltage variables [6–13], which also have the apparent form of Fick's laws [11,12].

Electrochemical modeling focuses on current–voltage relations, where common electrical signals consist of step currents, step voltages, linear sweep/scanning voltages, and sinusoidal current/voltages. All these signals can be found in classical electrochemistry books by Bard et al. [14,15]. Step current or voltage techniques are called constant-current chronopotentiometry and potential step chronoamperometry (PSCA), respectively, or simply chronopotentiometry or chronoamperometry. If a single current or voltage step is applied, the technique is commonly known as constant-current or constant-voltage charging/discharging in the battery field [16]. If the steps are performed sequentially, chronopotentiometry and chronoamperometry are classified as galvanostatic intermittent titration technique (GITT) [17] and potentiostatic intermittent titration technique (PITT) [18], respectively, by Huggins et al. The technique with a linear sweep voltage is called linear sweep voltammetry (LSV). If the sweeping is performed, both anodically and cathodically, it is called cyclic voltammetry (CV). Finally, the technique involving sinusoidal electrical signal is usually called impedance spectroscopy (IS) [19], dielectric spectroscopy (DS) [20], or electrochemical impedance spectroscopy (EIS) when applied to electrochemical systems [21].

While it is experimentally routine to apply several of the above-mentioned techniques simultaneously for the investigation of battery materials, (e.g. in Ref. [22]), some studies on numerical simulation only focus on one technique, such as constant current [23–25], potential step [26,27], linear sweep voltammetry [28,29],

* Tel.: +1 517 355 5126; fax: +1 517 432 1105.
  E-mail address: laiwei@msu.edu

Nomenclature

b	mobility
c	concentration
c^0	reference or maximum concentration
C^{chem}	chemical capacitance
$\tilde{D}$	chemical diffusivity
e	electron charge
f	dimensionless frequency
f_{exp}	experimental frequency
g	dimensionless interaction parameter
j	dimensionless current density
$\boldsymbol{J}$	current density
$\boldsymbol{J}^{ms}$	mass flux
k_B	Boltzmann constant
k_S	jump parameter in the solid
k_L	jump parameter in the liquid
m	planar, cylindrical, and spherical symmetry parameter
r	length
R	resistance
R_{int}	interfacial resistance
t	time
t_0	characteristic time
T	absolute temperature
V	voltage
x	position
X	dimensionless concentration
z	charge number

Greek letters

α	apparent symmetry factor
δ_{SL}	solid|liquid interfacial length
ε_0	vacuum permittivity
ε_r	relative permittivity
ϕ	electrical potential
γ	dimensionless interfacial energy
μ	chemical potential
μ^*	reduced chemical potential
$\tilde{\mu}$	electrochemical potential
$\tilde{\mu}^*$	reduced electrochemical potential
σ	conductivity
τ	dimensionless time
ω	angular frequency
ψ	dimensionless voltage

and impedance spectroscopy [30]. In these studies Fick's laws are almost invariably used with constant diffusivity. The application of constant diffusivity is based on the assumption of "small-signal" perturbations; however, it is not clear what magnitude should be considered "small". In addition, kinetic properties (diffusivity) and thermodynamic properties (chemical potential or voltage) are usually treated as two separate sets of data, while it is recognized that the evolution of systems (kinetics) is determined by the thermodynamic information under the context of irreversible thermodynamics [31].

This work seeks to provide a comprehensive numerical study on the current–voltage relationship of a single intercalation electrode particle with different thermodynamic properties. The thermodynamic model utilized a regular solution model or Frumkin adsorption isotherm, which will be discussed in Section 2.2. This study will consider three different cases, including a solid solution with constant diffusivity, a solid solution with variable diffusivity, and a phase transformation material. The evolution of the system, in

the form of the transport of ions and electrons, will be described by the generalized PNP equations in Section 2.1. Boundary conditions and dimensionless forms of involved partial different equations are described in Sections 2.3 and 2.4. Numerical simulation results for the four common electrical signals such asthe step current, step voltage, linear sweep voltage, and sinusoidal current, are presented in Section 3.

2. Models

The detailed discussion of the generalized PNP equations and the regular solution model can be found in references [11,12] and is included here for completeness.

2.1. Generalized Poisson–Nernst–Planck (PNP) equations

The classical PNP equations [1–4] are usually formulated as coupled partial differential equations that track concentration c_i, electrical potential ϕ, and mass flux $\boldsymbol{J}_i^{ms}$ as follows:

$$\boldsymbol{J}_i^{ms} = -\tilde{D}_i \nabla c_i - \frac{\sigma_i}{z_i e} \nabla \phi, \tag{1}$$

$$\frac{\partial c_i}{\partial t} + \nabla \cdot \boldsymbol{J}_i^{ms} = 0, \tag{2}$$

$$-\varepsilon_r \varepsilon_0 \Delta \phi = \sum_i z_i e c_i, \tag{3}$$

where $\tilde{D}_i$ is the chemical diffusivity, z_i is the charge number, e is the elementary electron charge, and ε_r and ε_0 are relative and vacuum permittivity, respectively. The conductivity σ_i is the product of concentration c_i and mobility b_i as follows:

$$\sigma_i = (z_i e)^2 c_i b_i. \tag{4}$$

For the dilute solution, these equations are known as drift-diffusion equations in semiconductor devices [3].

These constitutive equations in electrochemistry can be reformulated as generalized Poisson–Nernst–Planck equations [11,12]

$$\boldsymbol{J}_i = -\sigma_i \nabla \tilde{\mu}_i^*, \tag{5}$$

$$C_i^{chem} \frac{\partial \mu_i^*}{\partial t} + \nabla \cdot \boldsymbol{J}_i = 0, \tag{6}$$

$$\boldsymbol{J}_{dis} = -\frac{\partial}{\partial t}(\varepsilon_r \varepsilon_0 \nabla \phi), \tag{7}$$

$$\boldsymbol{J}_T = \boldsymbol{J}_{dis} + \sum_i \boldsymbol{J}_i. \tag{8}$$

This formulation was primarily discussed under the context of dilute solutions and impedance spectra reported in the past [6–10].

The correlation between the two formulations is given by several physically intuitive but less commonly used parameters. First, the current density $\boldsymbol{J}_i$, reduced electrochemical potential $\tilde{\mu}_i^*$, and reduced chemical potential μ_i^* are used in Eqs. (5)–(8), instead of the conventional mass flux $\boldsymbol{J}_i^{ms}$, electrochemical potential $\tilde{\mu}_i$, and chemical potential μ_i found in Eqs. (1)–(3). The relation is given by the following:

$$\boldsymbol{J}_i = z_i e \boldsymbol{J}_i^{ms}, \quad \tilde{\mu}_i = z_i e \tilde{\mu}_i^*, \quad \mu_i = z_i e \mu_i^*. \tag{9}$$

The electrochemical potential $\tilde{\mu}_i$ is the sum of chemical potential μ_i and electrical energy $z_i e \phi$ as follows:

$$\tilde{\mu}_i = \mu_i + z_i e \phi. \tag{10}$$

Thus, the reduced electrochemical potential has the form:

$$\tilde{\mu}_i^* = \mu_i^* + \phi. \tag{11}$$
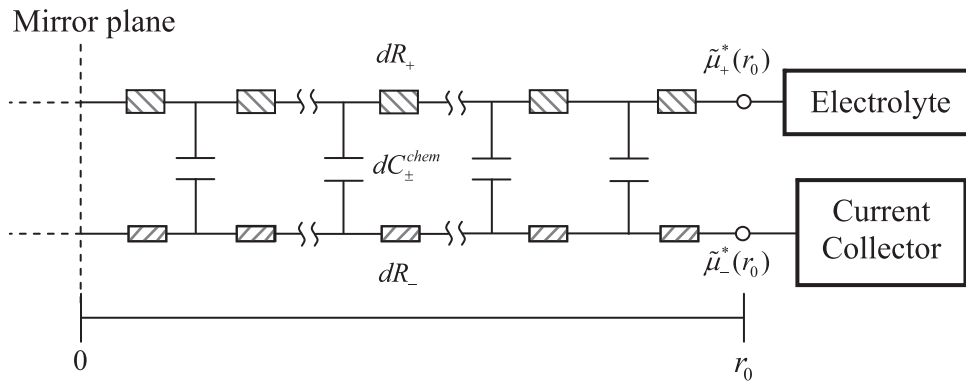
Mirror plane

Fig. 1. Equivalent circuit for a two-charge carrier (positive + and negative −) particle under electroneutrality conditions. 0 and r_0 are at the center and surface of the particle, respectively. Differential resistor (dR_+ and dR_-) and capacitor ($dC_\pm^{chem}$) elements are shown along with surface voltages $\tilde{\mu}_+^*(r_0)$ and $\tilde{\mu}_+^*(r_0)$.

Second, volumetric chemical capacitance C_i^{chem} represents the change of volumetric electrical charge $z_i e c_i$ upon a change of reduced chemical potential μ_i^*:

$$C_i^{chem} = z_i e \frac{\partial c_i}{\partial \mu_i^*}. \tag{12}$$

Third, chemical diffusivity $\tilde{D}_i$ is defined as the following:

$$\tilde{D}_i = \frac{\sigma_i}{C_i^{chem}}. \tag{13}$$

This new formulation, i.e. Eqs. (5)–(8), is based on a set of coupled partial differential equations that track the reduced electrochemical potential $\tilde{\mu}_i^*$, reduced chemical potential μ_i^*, electrical potential ϕ, current density J_i, displacement current density J_{dis}, and total current density J_T. Importantly, all the potential terms, $\tilde{\mu}_i^*$, μ_i^* and ϕ, contain units of voltage. This voltage–current (density) formulation is especially convenient for electrochemical modeling because voltage and current signals can be applied and measured for the experiments. It also allows the mapping of these differential equations to an equivalent circuit; thus, the physical meanings of the charge transport can be clearly understood [6–13]. Finally, a mixed formulation from Eqs. (1)–(3) and (5)–(8), with concentration c_i, reduced electrochemical potential $\tilde{\mu}_i^*$, electrical potential ϕ and current densities J_i, lead to equations that are similar to Newman's model [13,32].

For a two-charge-carrier (positive + and negative −) particle under electroneutrality condition, the generalized PNP equations (5)–(8) under planar ($m=0$), cylindrical ($m=1$), and spherical ($m=2$) symmetry become [11,12] the following:

$$J_+ = -\sigma_+ \frac{\partial \tilde{\mu}_+^*}{\partial r}, \tag{14}$$

$$J_- = -\sigma_- \frac{\partial \tilde{\mu}_-^*}{\partial r}, \tag{15}$$

$$\frac{\partial}{\partial r}(r^m J_+) = r^m C_\pm^{chem} \frac{\partial(\mu_-^* - \mu_+^*)}{\partial t}. \tag{16}$$

The combined chemical capacitance of the ion and electron $C_\pm^{chem}$ is the following:

$$\frac{1}{C_\pm^{chem}} = \frac{1}{C_+^{chem}} + \frac{1}{C_-^{chem}} = \frac{1}{e}\frac{\partial}{\partial c}(\mu_+^* - \mu_-^*). \tag{17}$$

These partial differential equations can be mapped to an equivalent circuit, as shown in Fig. 1. Here the two-charge system is a solid electrode particle with lithium ions (+) and electrons (−). The positions 0 and r_0 represent the center and surface of the particle, respectively. The two resistor rails correspond to the transport of two charge carriers, and the chemical capacitors represent

their coupling. The differential resistor (dR_+ and dR_-) and capacitor ($dC_\pm^{chem}$) elements are shown in Fig. 1.

The surface voltage $\tilde{\mu}_-^*(r_0)$ determines how lithium ions will be inserted or extracted from the electrolyte, and the surface voltage $\tilde{\mu}_+^*(L)$ determines how electrons will be inserted or extracted from the current collector. Thus, the variables of interest are the voltage difference $\tilde{\mu}_-^*(r_0) - \tilde{\mu}_+^*(r_0)$ and current density $J_+(r_0)$. In addition, Eqs. (14) and (15) can be written as follows:

$$J_+ - \frac{\sigma_+}{\sigma_-}J_- = \sigma_+ \frac{\partial}{\partial r}(\tilde{\mu}_-^* - \tilde{\mu}_+^*). \tag{18}$$

From the definition of Eq. (11), the difference of the reduced electrochemical potential is the same as that of the reduced chemical potential

$$\tilde{\mu}_-^* - \tilde{\mu}_+^* = \mu_-^* - \mu_+^*. \tag{19}$$

These equations can be simplified if two assumptions regarding the thermodynamics and kinetics are made. First, it is assumed that the chemical potential of electrons does not depend on their concentration. Essentially this leads to the position independent chemical potential, $\partial \mu_-^*/\partial r \approx 0$. Second, it is assumed that electronic mobility is much larger than ionic mobility; thus, electronic conductivity dominates over ionic conductivity under the electroneutrality condition, $\sigma_+/\sigma_- \approx 0$. With these two assumptions, Eqs. (18) and (19) become the following:

$$J_+^{ms} = -\frac{\sigma_+}{e}\frac{\partial \mu_+^*}{\partial r}. \tag{20}$$

Eq. (20) can also be written as the following:

$$J_+^{ms} = -\tilde{D}_+ \frac{\partial c_+}{\partial r} = -\frac{\sigma_+}{C_+^{chem}}\frac{\partial c_+}{\partial r}. \tag{21}$$

Here, the definitions of Eqs. (9), (12) and (13) are used. Eqs. (16) and (17) lead to the following equation:

$$r^m \frac{\partial c_+}{\partial t} = -\frac{\partial}{\partial r}(r^m J_+^{ms}). \tag{22}$$

Eqs. (21) and (22) have the same form as the well-known Fick's laws and can be called generalized diffusion equations. However, the present formulations presents the conditions to validate these equations. Second, it displays the relevant voltage variables. Third, it shows that the chemical diffusivity $\tilde{D}_+$ is related to the kinetic (conductivity σ_+) and thermodynamic (chemical capacitance C_+^{chem}) properties and could depend on the concentration c_+.
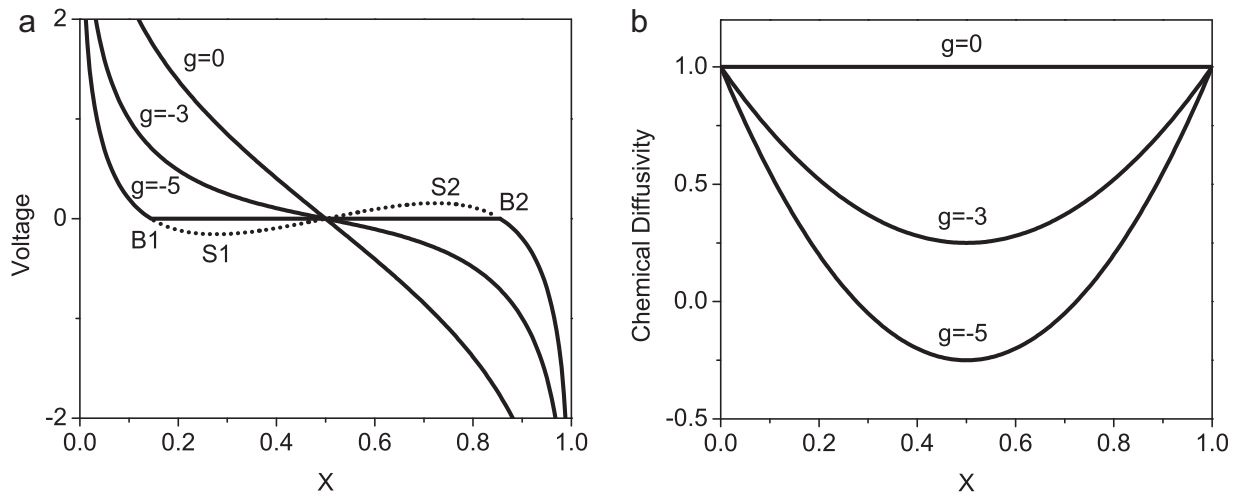
Fig. 2. (a) Dimensionless voltage $-\ln[X/(1-X)] - g(X-0.5)$ for three different thermodynamic parameters $g=0$, $g=-3$, and $g=-5$. B1 and B2 are binodal points and S1 and S2 are spinodal points. (b) Dimensionless chemical diffusivity $1+gX(1-X)$ for three different thermodynamic parameters.

2.2. Regular solution model

A regular solution is a thermodynamic model that describes a binary AB solution [33,34]. It is also called the Frumkin adsorption isotherm [35–37], in which the gas species and empty solid surface sites can be considered as A and B, respectively. In lithium intercalation materials, lithium ions in the polyhedral sites will be denoted A and empty intercalation sites will be denoted B. In the present notation, the chemical potential of lithium ions is as follows:

$$\mu_+ = \mu_+^0 + k_B T \ln \frac{X}{1-X} + k_B T g (X-0.5), \quad X = \frac{c_+}{c_+^0}. \tag{23}$$

The first term on the right hand side μ_+^0 is the standard chemical potential. The second term is the entropic contribution, where k_B is the Boltzmann constant and T is the absolute temperature. The third term is the interaction term that accounts for the interaction between A–A, B–B and A–B couples, where g is a dimensionless interaction parameter. Variable c_+^0 is the maximum concentration and X is the dimensionless concentration. For this regular solution model, the volumetric chemical capacitance becomes the following:

$$C_+^{chem} = e \frac{\partial c_+}{\partial \mu_+^*} = \frac{e^2 c_+^0}{k_B T} \left[\frac{1}{X} + \frac{1}{1-X} + g \right]^{-1}. \tag{24}$$

For the kinetics of jumps, the lithium ion mobility depends on whether the potential jump site is empty, as follows:

$$b_+ = b_+^0 (1-X), \tag{25}$$

where b_+^0 is a constant. This is different from the mobility expression of reference [38,39], in which the mobility is considered a constant. The conductivity then becomes the following:

$$\sigma_+ = e^2 c_+ b_+ = \frac{D_+^0 c_+^0 e^2}{k_B T} X(1-X), \tag{26}$$

where

$$D_+^0 = k_B T b_+^0. \tag{27}$$

Thus, the chemical diffusivity takes the form of following equation:

$$\tilde{D}_+ = \frac{\sigma_+}{C_+^{chem}} = D_+^0 [1 + gX(1-X)]. \tag{28}$$

As reported in Ref. [11], it is informative to plot the dimensionless voltage $-\ln[X/(1-X)] - g(X-0.5)$ in Eq. (23) and the

dimensionless chemical diffusivity $1+gX(1-X)$ in Eq. (28) for different values of interaction parameters g. Three g values, 0, −3, and −5, are plotted in Fig. 2. The Langmuir adsorption isotherm corresponds to the case of $g=0$. When g is less than −4, both the chemical capacitance C_+^{chem} and the chemical diffusivity $\tilde{D}_+$ take a negative value at intermediate X values as can be seen in Fig. 2(b). Because chemical capacitance is essentially the second order derivative of free energy with respect to X, this system is unstable and the initial homogeneous system will separate into two phases [34,40] when g is less than −4. In the two-phase coexistence region, the chemical potential is fixed so that the equilibrium thermodynamic curve becomes the solid line for $g=-5$ in Fig. 2(a). The dotted line is described by Eq. (23). The two ends of this dotted line, B1 and B2, are called binodal points and have values of approximately 0.145 and 0.855, respectively. The local minimum and maximum points, S1 and S2, are called spinodal points and are approximately 0.276 and 0.724, respectively. The regions between B1 and S1 and between S2 and B2, are metastable. The region between S1 and S2 is the unstable spinodal region. When g is equal to −4, the chemical capacitance goes to infinity, and the chemical diffusivity goes to 0 at $X=0.5$ (Fig. 2(b)), which was discussed in Ref. [11].

In this study, the regular solution model with $g=0$, $g=-3$, and $g=-5$ was chosen to represent a solid solution with constant diffusivity, a solid solution with variable diffusivity, and a phase transformation material, respectively. During phase transformation, a phase boundary develops and moves between coexisting phases. In the present work, a diffuse interface model using the phase field method was utilized to study the movement of the phase boundary. In addition to its widespread application in solidification and morphology evolution [41–44], the phase field method has recently been applied in a few works to the study of electrochemistry in the context of electrodeposition [45,46] and phase transformation in battery electrodes [38,39,47–49].

In the phase field method, the chemical potential [39] is represented by the following:

$$\mu_+ = \mu_+^0 + k_B T \ln \frac{X}{1-X} + k_B T g (X-0.5)$$
$$- k_B T \gamma r_0^2 \frac{1}{r^m} \frac{\partial}{\partial r} \left(r^m \frac{\partial X}{\partial r} \right). \tag{29}$$

Compared to Eq. (23), the extra fourth term is the Cahn–Hilliard interfacial energy term [50], where γ is the dimensionless interfacial energy parameter. This term goes to 0 in the case of solid solutions with $g=0$ and $g=-3$, i.e. Eq. (23). The term γ is taken to
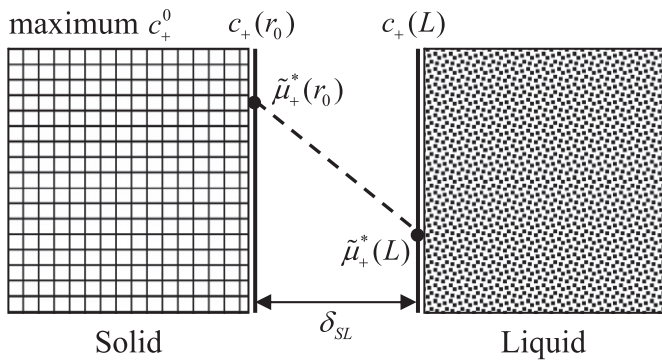
Fig. 3. Schematic depiction of interfacial ionic transport at the solid|liquid interface. The relevant concentrations c_+ and reduced electrochemical potentials $\tilde{\mu}_+^*$ of the solid and liquid are labeled along with the interfacial length δ_{SL}.

be 10^{-5} in this work. This interfacial parameter is related to the interface between two coexisting phases in the solid, but not to the solid|liquid interface to be discussed shortly.

2.3. Boundary conditions

If the solid electrode particle is in contact with the liquid electrolyte, the transport of lithium ions occurs across the solid|liquid interface. The latter is shown schematically in Fig. 3, where the interfacial length is δ_{SL}. Variables $c_+(r_0)$ and $c_+(L)$ are the lithium ion concentrations in the solid and liquid, respectively, on the two sides of the interface. The driving force is the difference between the reduced electrochemical potentials of lithium ions, $\tilde{\mu}_+^*(r_0)$ and $\tilde{\mu}_+^*(L)$. The jump is assumed to exponentially depend on the driving force as an Arrhenius rate expression. The jumping probability also depends on the direction. Specifically, jumping from liquid to solid, the jump rate is proportional to the fraction of available sites given by $1 - X(r_0)$, while the jump from solid to liquid has no such restriction.

Thus, the current density from solid to liquid and liquid to solid can be written as follows:

$$J_{SL} = \frac{k_S}{\delta_{SL}} X(r_0) \exp\left[\frac{\tilde{\mu}_+^*(r_0) - \tilde{\mu}_+^*(L)}{k_B T/e}\right], \tag{30}$$

$$J_{LS} = \frac{k_L}{\delta_{SL}} \frac{c_+(L)}{c_+^0}[1 - X(r_0)] \exp\left[\frac{\tilde{\mu}_+^*(L) - \tilde{\mu}_+^*(r_0)}{k_B T/e}\right], \tag{31}$$

where k_s and k_L are parameters that incorporate the jumping probabilities. Combining bidirectional fluxes, the current density across this interface from solid to liquid can be written as follows:

$$J_+(r_0) = \frac{k_S}{\delta_{SL}} X(r_0) \exp\left[\frac{\tilde{\mu}_+^*(r_0) - \tilde{\mu}_+^*(L)}{k_B T/e}\right]$$
$$- \frac{k_L}{\delta_{SL}} \frac{c_+(L)}{c_+^0}[1 - X(r_0)] \exp\left[-\frac{\tilde{\mu}_+^*(r_0) - \tilde{\mu}_+^*(L)}{k_B T/e}\right]. \tag{32}$$

Clearly, the application of the above rationale to the jump from position x to $x + dx$ in the solid provides the following equation:

$$J_+ = \frac{k(x)}{dx} X(x)[1 - X(x+dx)] \exp\left[\frac{\tilde{\mu}_+^*(x) - \tilde{\mu}_+^*(x+dx)}{k_B T/e}\right]$$
$$- \frac{k(x+dx)}{dx} X(x+dx)[1 - X(x)] \exp\left[-\frac{\tilde{\mu}_+^*(x) - \tilde{\mu}_+^*(x+dx)}{k_B T/e}\right]. \tag{33}$$

As dx goes to 0, Eq. (33) can be written as the following:

$$J_+ = -2k(r)X(r)[1 - X(r)]\frac{d\tilde{\mu}_+^*(r)}{dr}. \tag{34}$$

This expression is consistent with Eqs. (5) and (26), as shown before.

At the solid|liquid interface, the expression of Eq. (32) can be simplified in different ways. First, it can be written as the following:

$$J_+(r_0) = J_0 \left\{ \exp\left[\alpha\frac{\tilde{\mu}_+^*(r_0) - \tilde{\mu}_+^*(L)}{k_B T/e}\right] - \exp\left[-\alpha\frac{\tilde{\mu}_+^*(r_0) - \tilde{\mu}_+^*(L)}{k_B T/e}\right] \right\}$$
$$= 2J_0 \sinh\left[\alpha\frac{\tilde{\mu}_+^*(r_0) - \tilde{\mu}_+^*(L)}{k_B T/e}\right]. \tag{35}$$

This equation has a form similar to that of the Butler–Volmer equation [14,51–53]. The apparent exchange current density J_0 and symmetry factor α can be represented as the following:

$$J_0 = \sqrt{\frac{k_S}{\delta_{SL}} X(r_0) \frac{k_L}{\delta_{SL}} \frac{c_+(L)}{c_+^0}}[1 - X(r_0)], \tag{36}$$

$$\alpha = 1 + \frac{1}{2} \frac{k_B T/e}{\tilde{\mu}_+^*(r_0) - \tilde{\mu}_+^*(L)} \ln \frac{k_S X(r_0)}{k_L [1 - X(r_0)] c_+(L)/c_+^0}. \tag{37}$$

This formulation is also similar to the symmetrized form of the transport equation under a large gradient driving force [54]. Because the classical Butler–Volmer equation can be approximated by the Tafel and linearized equations [14], two similarly simplified forms of the generalized Butler–Volmer equation, Eq. (35), can be obtained as de Donder's equation and the resistive equation, respectively. First, if the argument in the hyperbolic sine function is large and positive, Eq. (35) can be written as follows:

$$J_+(r_0) = J_0 \left\{ \exp\left[\alpha\frac{\tilde{\mu}_+^*(r_0) - \tilde{\mu}_+^*(L)}{k_B T/e}\right] - 1 \right\}. \tag{38}$$

This equation has the form of de Donder's equation, as in Ref. [47]. The term of 1 in the curly bracket can be ignored because it is much smaller than the exponential term and it provides the Tafel form [14].

Second, if the term in the hyperbolic sine function of Eq. (35) is small, it can be linearized as follows:

$$J_+(r_0) = \frac{2\alpha J_0}{k_B T/e}[\tilde{\mu}_+^*(r_0) - \tilde{\mu}_+^*(L)]. \tag{39}$$

This equation can be called the generalized Chang–Jaffe equation. In the conventional Chang–Jaffé equation [55], the term in front of the square bracket is a constant, and the difference term inside the square bracket is the concentration difference. Furthermore, if the term before the square bracket is assumed to be a constant, Eq. (39) becomes the following:

$$J_+(r_0) = \frac{\tilde{\mu}_+^*(r_0) - \tilde{\mu}_+^*(L)}{R_{\text{int}}}. \tag{40}$$

where R_{int} is a constant. This expression was used in the study of interfaces involving mixed conductors [10,56,57] and can be called a resistive/ohmic boundary condition. This was also called the cell-impedance-controlled boundary condition [58]. When R_{int} is small, it is expected that variable $\tilde{\mu}_+^*(r_0) - \tilde{\mu}_+^*(L)$ will also be small; this can be called the reversible boundary condition. In this case, $J_+(r_0)$ can be determined by the "diffusion equations", i.e. Eqs. (20) and (22), which relate J_+ to $\tilde{\mu}_+^*(r_0)$; this can be called a diffusion-controlled mechanism. When R_{int} is large, it can be called an interface-controlled mechanism or kinetics-controlled with ohmic behavior. For intermediate values of R_{int}, it can be called a mixed-controlled mechanism [26].

Eq. (40) is the interfacial solid|liquid boundary condition that is employed in the present study and is equivalent to replacing the

electrolyte box with a resistor in Fig. 1. At the other boundary, i.e. the particle center, the flux is zero due to symmetry, as is described below:

$$J_+(0) = 0. \tag{41}$$

Finally, in Fig. 1, the voltage difference $\tilde{\mu}_-^*(r_0) - \tilde{\mu}_+^*(L)$ was used as the external voltage V_{ext} and the current density $J_+(r_0)$ was used as the external current. Thus, Eq. (40) was transformed to become the following:

$$J_+(r_0) = \frac{\mu_+^*(r_0) - \mu_-^*(r_0) + V_{ext}}{R_{int}} \tag{42}$$

The equivalence of reduced electrochemical potential difference to reduced chemical potential difference, Eq. (19), was once again applied. In addition, the initial conditions were always set to the open circuit, where the current was 0 and the voltage was the open circuit voltage $V_{ext}(0)$:

$$V_{ext}(0) = \mu_-^*(r_0, t = 0) - \mu_+^*(r_0, t = 0) \tag{43}$$

The voltage difference $\Delta V = V_{ext} - V_{ext}(0)$ after the current or voltage perturbation obeyed the following equation:

$$J_+(r_0) = \frac{\mu_+^*(r_0) - \mu_+^*(r_0, t = 0) + \Delta V}{R_{int}}. \tag{44}$$

Here, the chemical potential of electrons is a constant as mentioned before.

For convenience, the partial differential equations, Eqs. (20) and (22), along with the boundary conditions, Eqs. (41) and (44), and expressions of relevant parameters, Eqs. (26) and (29), are listed below:

$$\begin{aligned} J_+^{ms} &= -\frac{\sigma_+}{e} \frac{\partial \mu_+^*}{\partial r} \\ r^m \frac{\partial c}{\partial t} &= -\frac{\partial}{\partial r}(r^m J_+^{ms}) \\ J_+^{ms}(0) &= 0 \\ J_+^{ms}(r_0) &= \frac{\mu_+^*(r_0) - \mu_+^*(r_0, t = 0) + \Delta V}{e R_{int}} \\ \sigma_+ &= \frac{D_+^0 c_+^0 e^2}{k_B T} X(1 - X) \\ \mu_+ &= \mu_+^0 + k_B T \ln \frac{X}{1 - X} + k_B T g(X - 0.5) \\ &\quad - k_B T \gamma r_0^2 \frac{1}{r^m} \frac{\partial}{\partial r}\left(r^m \frac{\partial X}{\partial r}\right) \end{aligned} \tag{45}$$

2.4. Dimensionless form

For numerical simulations, it is convenient to use the following dimensionless variables:

$$X = \frac{c_+}{c_+^0}, \quad x = \frac{r}{r_0}, \quad \tau = \frac{t}{t_0}, \quad j = \frac{J_+^{ms}}{c_+^0 r_0 / t_0}, \quad \psi = -\frac{\mu_+ - \mu_+^0}{k_B T},$$

$$R = \frac{R_{int}}{k_B T r_0 / (D_+^0 c_+^0 e^2)}, \quad \Delta v = \frac{e \Delta V}{k_B T}. \tag{46}$$

The characteristic time t_0 is represented by the following:

$$t_0 = \frac{r_0^2}{D_+^0}. \tag{47}$$

Then, Eq. (45) becomes the following:

$$\begin{aligned} j &= X(1 - X)\frac{\partial \psi}{\partial x} \\ x^m \frac{\partial X}{\partial \tau} &= \frac{\partial}{\partial x}(-x^m j) \\ \psi &= -\left[\ln \frac{X}{1 - X} + g(X - 0.5) - \gamma \frac{1}{x^m} \frac{\partial}{\partial x}\left(x^m \frac{\partial X}{\partial x}\right)\right]. \\ j(0) &= 0 \\ j(1) &= \frac{\psi(1, \tau = 0) - \psi(1) + \Delta v}{R} \end{aligned} \tag{48}$$

where $\psi(1, t = 0) + \Delta v$ is the voltage in the liquid and $\psi(1)$ is the voltage on the solid surface. The goal of the present work is to find the relation between $j(1)$ and $\psi(1, \tau = 0) + \Delta v$.

In the battery field, a commonly used notation for current is the C rate. C/n is the current that takes n hours to fully charge or discharge a battery. For a single particle with maximum concentration c_+^0, the mass flux density corresponding to the C/n rate becomes the following:

$$J_+^{ms} = \frac{c_+^0 r_0}{(m + 1)n \cdot 3600}. \tag{49}$$

Then, the dimensionless mass flux density in C rate is described as the following:

$$j = \frac{1}{m + 1} \frac{t_0}{3600n}. \tag{50}$$

For example, a dimensionless flux of 1 through the surface of a planar ($m = 0$) particle corresponds to the C or $C/10$ rates, when the characteristic time t_0 is 1 h or 10 h, respectively.

2.4.1. Phase transformation material

For the phase transformation material, Eq. (48) becomes the following:

$$\psi = -\left[\ln \frac{X}{1 - X} + g(X - 0.5) - \gamma \frac{1}{x^m} \frac{\partial}{\partial x}\left(x^m \frac{\partial X}{\partial x}\right)\right], \tag{51}$$

$$x^m \frac{\partial X}{\partial \tau} = \frac{\partial}{\partial x}\left[-x^m X(1 - X)\frac{\partial \psi}{\partial x}\right]. \tag{52}$$

Eqs. (51) and (52) are two coupled second-order partial differential equations on X and ψ. For Eq. (51), the boundary conditions are the following:

$$\gamma \frac{\partial X(0)}{\partial x} = \gamma \frac{\partial X(1)}{\partial x} = 0. \tag{53}$$

This indicates that phase transformation will not occur (zero interfacial energy between two phases) at the center and at the surface of the particle [47]. The boundary conditions for Eq. (52) are the last two equations in Eq. (48).

2.4.2. Solid solution material

For the solid solution material, the second order partial differential equation Eq. (51) becomes the following expression:

$$\psi = -\left[\ln \frac{X}{1 - X} + g(X - 0.5)\right]. \tag{54}$$

Because it does not involve partial derivatives, Eq. (52) becomes the following:

$$x^m \frac{\partial X}{\partial \tau} = \frac{\partial}{\partial x}\left[x^m [1 + gX(1 - X)]\frac{\partial X}{\partial x}\right]. \tag{55}$$

This is the same second order partial differential equation used in the present author's previous work [11].

Table 1
Partial differential equations along with parameters used in thermodynamics, initial conditions (IC), and boundary conditions (BC).

$j = X(1-X)\frac{\partial \psi}{\partial x}$		$x^m \frac{\partial X}{\partial \tau} = \frac{\partial}{\partial x}(-x^m j)$	$\psi = -\left[\ln \frac{X}{1-X} + g(X - 0.5) - \gamma \frac{1}{x^m}\frac{\partial}{\partial x}\left(x^m \frac{\partial X}{\partial x}\right)\right]$	
		Solid solution $g = 0,\ \gamma = 0$	Solid solution $g = -3,\ \gamma = 0$	Phase transformation $g = -5,\ \gamma = 10^{-5}$
Step current	IC	$X_0 = 0.99$	$\psi(1, \tau = 0) = -\ln[X_0/(1-X_0)] - g(X_0 - 0.5)$	
	BC	$\gamma \frac{\partial X(0)}{\partial x} = \gamma \frac{\partial X(1)}{\partial x} = 0$	$j(0) = 0$	$j(1) = 0.05,\ 0.1,\ 0.2,\ 0.5$
Step voltage	IC	$X_0 = 0.9$	$\psi(1, \tau = 0) = -\ln[X_0/(1-X_0)] - g(X_0 - 0.5)$	
	BC	$\gamma \frac{\partial X(0)}{\partial x} = \gamma \frac{\partial X(1)}{\partial x} = 0$	$j(0) = 0$	$j(1) = \frac{\psi(1,\tau=0)-\psi(1)+\Delta v}{R}$, $\Delta v = 0.5,\ 1,\ 2,\ 5;\ R = 0.1,\ 1,\ 10$
Linear sweep voltage	IC	$X_0 = 0.99$	$\psi(1, \tau = 0) = -\ln[X_0/(1-X_0)] - g(X_0 - 0.5)$	
	BC	$\gamma \frac{\partial X(0)}{\partial x} = \gamma \frac{\partial X(1)}{\partial x} = 0$	$j(0) = 0$	$j(1) = \frac{\psi(1,\tau=0)-\psi(1)+v^{LSV}\tau}{R}$, $v^{LSV} = 0.05,\ 0.1,\ 0.2,\ 0.5,\ 1;$ $R = 0.1,\ 1,\ 10$
Sinusoidal current	IC	$X_0 = 0.9$	$\psi(1, \tau = 0) = -\ln\left[\frac{X_0}{1-X_0}\right] - g(X_0 - 0.5)$	
	BC	$\gamma \frac{\partial X(0)}{\partial x} = \gamma \frac{\partial X(1)}{\partial x} = 0$	$j(0) = 0$	$j(1) = j_{AC}\sin(2\pi f\tau)$, $j_{AC} = 0.0001,\ 0.001,\ 0.01,\ 0.05;$ $f = 0.05 - 1000$

Unless otherwise specified, the initial condition is chosen as a constant concentration profile as follows:

$$X(x, \tau = 0) = X_0, \tag{56}$$

$$\psi(x, \tau = 0) = -\left[\ln \frac{X_0}{1 - X_0} + g(X_0 - 0.5)\right]. \tag{57}$$

The above partial differential equations are solved with Comsol Multiphysics software [59]. The dimensionless spatial grid is uniform, fixed in time, and composed by 500 segments. It was found the solution converges between 500 and 5000 elements, with the exception of some cases in impedance spectroscopy (details to be discussed later). The equations are solved using the finite element method with a Lagrange quadratic basis, ensuring quadratic convergence of the spatial discretization. In time the problem is solved using implicit finite backward finite differences of variable order.

3. Results and discussion

Before presenting the numerical results of Eq. (48), the known small-signal analytical solutions [12,30] are discussed. The first two partial differential equations in Eq. (48) can be formally rewritten as the following:

$$x^m \frac{\partial X}{\partial \psi}\frac{\partial \psi}{\partial \tau} = \frac{\partial}{\partial x}\left[-x^m X(1-X)\frac{\partial \psi}{\partial x}\right]. \tag{58}$$

A small perturbation of any form of $j(1)$ will likely cause small changes in X and ψ. If both $\partial \psi / \partial X$ and $X(1-X)$ are assumed to be constant during the course of perturbation and initial concentration profile is uniform X_0, perturbations of Eq. (58) yield the following:

$$
\begin{aligned}
x^m \frac{\partial \Delta \psi}{\partial \tau} &= \left[-\left.\frac{\partial \psi}{\partial X}\right|_{X_0} X_0(1 - X_0)\right]\left(x^m \frac{\partial \Delta \psi}{\partial x}\right) \\
&= \tilde{D}(X_0)\frac{\partial}{\partial x}\left(x^m \frac{\partial \Delta \psi}{\partial x}\right),
\end{aligned}
\tag{59}
$$

where the change of voltage $\Delta \psi$ is the variable of interest and $\tilde{D}(X_0)$ has the following form:

$$\tilde{D}(X_0) = 1 + gX_0(1 - X_0). \tag{60}$$

After the Laplace transformation with boundary condition $j(0) = 0$ [12,30], in the planar case ($m = 0$), Eq. (59) can be solved to provide the following:

$$\frac{\overline{\Delta\psi(1)}(s)}{\overline{j(1)}(s)} = \frac{1}{X_0(1 - X_0)}\frac{\cosh \sqrt{s/\tilde{D}(X_0)}}{\sqrt{s/\tilde{D}(X_0)}}, \tag{61}$$

where the overbar represents the Laplace transformed variable, and s is a complex argument. The time-domain current/voltage perturbation signal, e.g. current step or voltage step, can be transformed to the Laplace domain, and then, Eq. (61) can be inversely transformed back to the time domain to obtain the corresponding
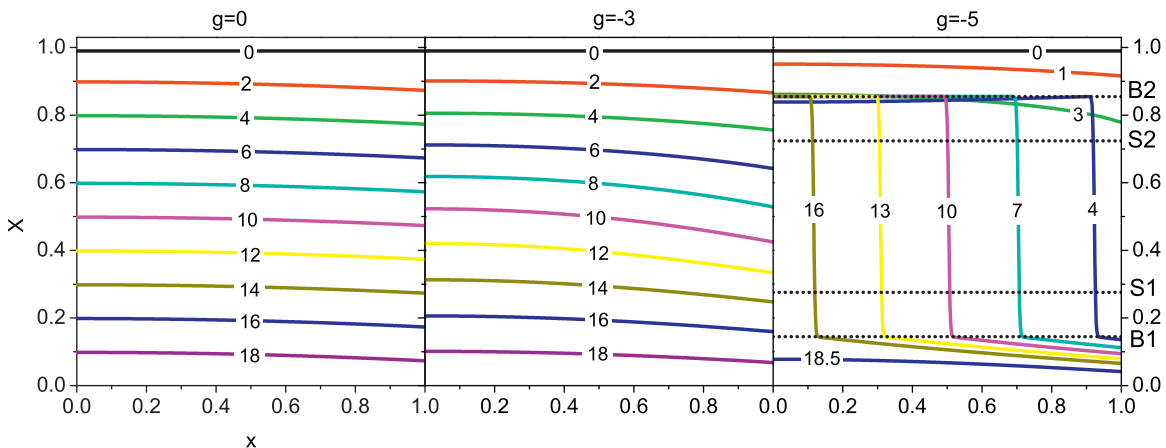

Fig. 4. Evolution of the concentration profile under a constant charging current $j(1)$ of 0.05 for three different thermodynamic parameters $g = 0$, $g = -3$, and $g = -5$. Dimensionless times are shown on each curve. B1, B2, S1, and S2 points are the binodal and spinodal points discussed in Section 2.2. Particle surface and center are at the position of 1 and 0, respectively.

voltage/current signal. When $s = i\omega$, where i is the imaginary number and ω is the angular frequency, the Laplace transform becomes the Fourier transform and Eq. (61) provides the impedance. Short-time and long-time analytical expressions obtained from Eq. (61) for the current step (Section 3.1), voltage step (Section 3.2), and sinusoidal current (Section 3.4) signals were compared with numerical results for signals of an arbitrary magnitude.

For the ease of comparison, parameters of thermodynamic parameters, initial conditions (IC), and boundary conditions (BC) used in the various techniques of Sections 3.1–3.4, are listed in Table 1, along with partial different equations that were solved.

3.1. Constant-current chronopotentiometry

In the constant-current chronopotentiometry study, a constant current $j(1)$ was applied and the voltage was monitored as a function of time. As discussed in Section 2.4, for the present single particle, voltage in the liquid $\psi(1, \tau = 0) + \Delta v$ was the variable of interest. However, because the solid surface was connected to the liquid by a resistor, the extra voltage difference could be easily obtained by multiplying resistance with the constant current. Thus, the voltage at the particle surface $\psi(1)$ was studied instead and this also applied to the controlled-current impedance spectroscopy in Section 3.4.

Initially, the concentration X_0 was a uniform value of 0.99 in the solid, and the simulation was performed in the charging process for a cathode particle. The current values $j(1)$ were 0.05, 0.1, 0.2, and 0.5 in dimensionless form. The time stepping ended when the surface concentration $X(1)$ reached 0.01. The time step was 0.005 for a current value of 0.5; otherwise, the time step was 0.02.

The evolution of the concentration profiles in the solid under a constant current of 0.05 is shown in Fig. 4. In the case of solid solutions with $g = 0, -3$, the concentration on the surface $x = 1$ decreased under the application of a constant charging current and gradually diffused into the center. In the case of the phase transformation material with $g = -5$, the area defined by the two inner horizontal dotted lines (S1 and S2) represents the unstable spinodal region, as discussed in Section 2.2. The two shells formed by the inner dotted lines and outer dotted lines (B1 and S1; S2 and B2) are the metastable regions. Clearly, the evolution of the concentration profile was similar to that in the solid solution before reaching the unstable region $X = 0.724$ ($\tau < 4$). Then, phase separation started and the phase boundary moved towards the center of the particle ($4 \leq \tau \leq 16$). Finally, the particle was in another single-phase region for $\tau \geq 18.5$.

It was interesting to study how fast the phase boundary moved and how this process depended on the current. The position and velocity of the phase boundary at different currents (0.05, 0.1, 0.2, and 0.5) are shown in Fig. 5. First, Fig. 5(a) indicates that it moved linearly with time for the current values investigated:

$$x_{PB}^{CC} \approx x_0^{CC} + v_{PB}^{CC}\tau, \tag{62}$$

where x_{PB}^{CC} and v_{PB}^{CC} are the phase boundary position and velocity respectively. Variable x_0^{CC} is a constant. Fitting the x_{PB}^{CC} data to Eq. (62) yielded v_{PB}^{CC}, and it was plotted as a function of current in Fig. 5(b). The phase boundary moved faster under higher current, as intuitively expected.

The capacity-voltage results are shown in Fig. 6. The capacity, the product of current $j(1)$ and time τ, was used to fit the battery field convention. The thermodynamic curves in Fig. 2 are also plotted in dashed lines as a reference. As the applied current increased from 0, polarization increased for all three thermodynamic cases, as expected. In addition, the voltage overshoot was observed at the beginning of charging process in the phase transformation case. Fig. 4 shows that surface concentration entered the metastable

region, e.g. at $\tau = 3$, before it reached the unstable region. As can be seen from Fig. 2(a), the concentration in the metastable region corresponded to a voltage overshoot beyond the voltage plateau. This overshoot has been experimentally observed for $LiCoO_2$ as it goes through the insulator-metal or O3-I to O3-II phase transition [60–62] and for the triphylite–heterosite phase transition of $LiFePO_4$ [63].

Finally, the small-signal solution under the context of GITT are discussed. For the constant current $j(1)$, the short-time voltage response can be obtained from the Laplace-inverse Laplace transformation of Eq. (61) [12,30]:

$$\frac{\Delta\psi(1)}{\sqrt{\tau}} = \frac{2j(1)}{X_0(1-X_0)}\sqrt{\frac{\tilde{D}(X_0)}{\pi}}, \tag{63}$$

where the right-hand side is a constant. This is similar to the expression in the GITT Ref. [17]. Results of plotting short-time ($\tau < 1$) data of Fig. 6 in the form of Eq. (63) are shown in Fig. 7. This equation did not hold even for the lowest current of 0.05, which suggested that the small-signal approximation is not satisfied at this current. However, this approximation is valid for a different initial condition that will be discussed in Section 3.5.

3.2. Potential step chronoamperometry

In the potential step chronoamperometry, a constant voltage step Δv was applied and the current $j(1)$ was monitored as a function of time. The boundary condition for $j(1)$ in Eq. (48) and three R values, 0.1, 1, and 10, were studied. These values were chosen to study different mechanisms, such as diffusion control, mixed control, and interface control.

Initially, the concentration X_0 was a uniform value of 0.9 in the solid, and the simulation was performed in the charging process. The voltage steps Δv were 0.2, 0.5, 1, 2, and 5. The time was incremented in steps 0.02 till $j(1)$ fell below 0.001.

Similar to the case of constant-current chronopotentiometry, the evolution of concentration profiles was studied first. Fig. 8 shows an example of the case with $\Delta v = 0.5$ and $R = 1$. If there was no solid|liquid interface, the voltage step implied that surface concentration was fixed, as in Ref. [11]. With an interface, the voltage step translated to a variable concentration step. Overall, the concentration steps led to steeper concentration profiles compared to the current steps, in solid solutions of $g = 0, -3$ in Fig. 4. In the case of phase transformation with $g = -5$, the change in the concentration profile under constant potential was similar to the case of constant current in Fig. 4. A voltage step of 0.5 eventually changed the surface from the high concentration phase to a low concentration phase, which was accompanied by the phase boundary movement towards the center. For the smallest voltage step of 0.2, no phase transformation was initiated.

Again, the positions of the phase boundary were tracked (Fig. 9(a)) with different voltage step Δv values and interfacial resistance R values. The phase boundary moved linearly with the square root of time:

$$x_{PB}^{CV} \approx x_0^{CV} + v_{PB}^{CV}\tau^{0.5}, \tag{64}$$

where x_{PB}^{CV} and v_{PB}^{CV} are phase boundary position and velocity constant, respectively. Variable x_0^{CV} is a constant. As the interfacial resistance was increased, e.g. $R = 10$, the square root dependence became less obvious. Fitting the x_{PB}^{CV} data to Eq. (64) yielded v_{PB}^{CV}, and it was plotted as a function of the voltage step in Fig. 9(b). The phase boundary moved faster under larger voltage steps, as intuitively expected. In addition, the phase boundary velocity showed little variation between $R = 0.1$ and $R = 1$, which suggested that both cases were diffusion-controlled. It can be expected that $R = 10$ would correspond to a mixed-controlled mechanism, and larger
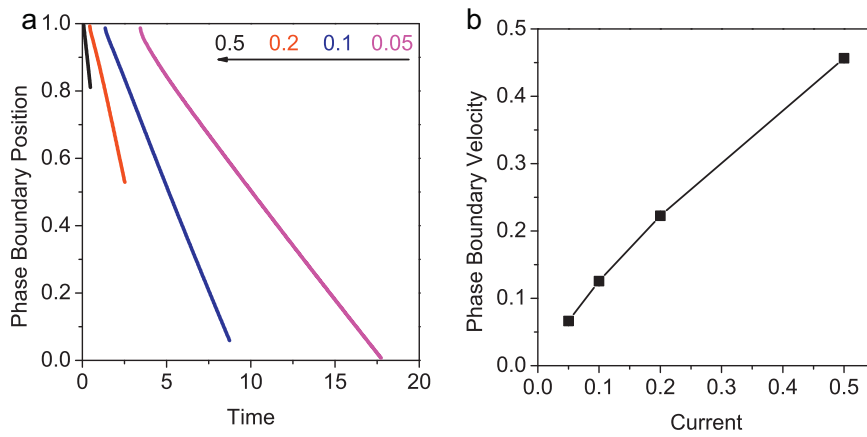
Fig. 5. (a) Phase boundary positions, and (b) phase boundary velocities under different values of constant current $j(1)$ (0.05, 0.1, 0.2, and 0.5) for the phase transformation material with $g = -5$.
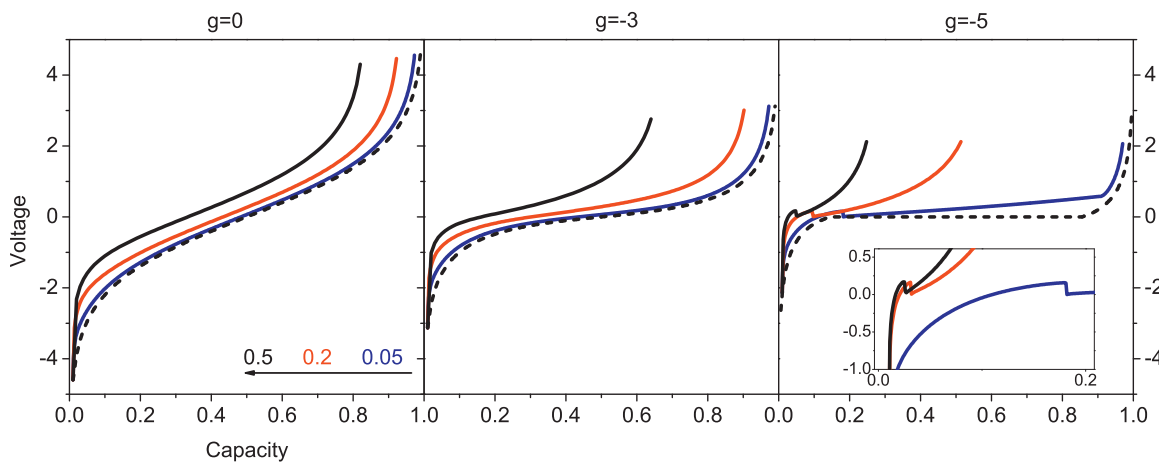

Fig. 6. Voltage $\psi(1)$ as a function of capacity under three different currents $j(1)$ (0.05, 0.2 and 0.5) for three different thermodynamic parameters $g = 0$, $g = -3$, and $g = -5$. Dashed lines represent the thermodynamic voltage curve in Fig. 2(a). The voltage overshoot can be clearly observed in the inset of $g = -5$.

R values would lead to an interface-controlled mechanism. As R became larger, e.g. 100, the linear time dependence was observed at long time periods (not shown). In the sharp-interface moving boundary model, the square root and linear dependences were also obtained for diffusion control and interface control mechanisms, respectively [64].

Finally, the relation between the voltage step Δv and current response $j(1)$ are shown. First, small-signal analytical expressions from Eq. (61) are discussed. If no interface effect was present, Δv was equivalent to $\Delta \psi(1)$. The short-time (Eq. (65)) and long-time (Eq. (66)) responses of the current $j(1)$ were obtained from the
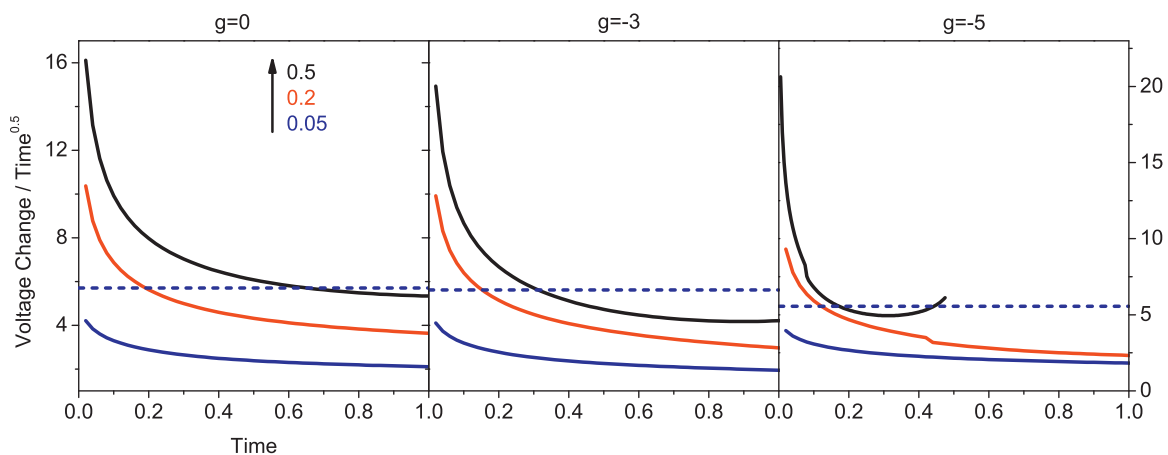
Fig. 7. Short-time characteristic curves according to Eq. (63) under three different currents $j(1)$ (0.05, 0.2 and 0.5) for three different thermodynamic parameters $g = 0$, $g = -3$, and $g = -5$. Dashed lines are the plateaus expected from the small-signal assumption.
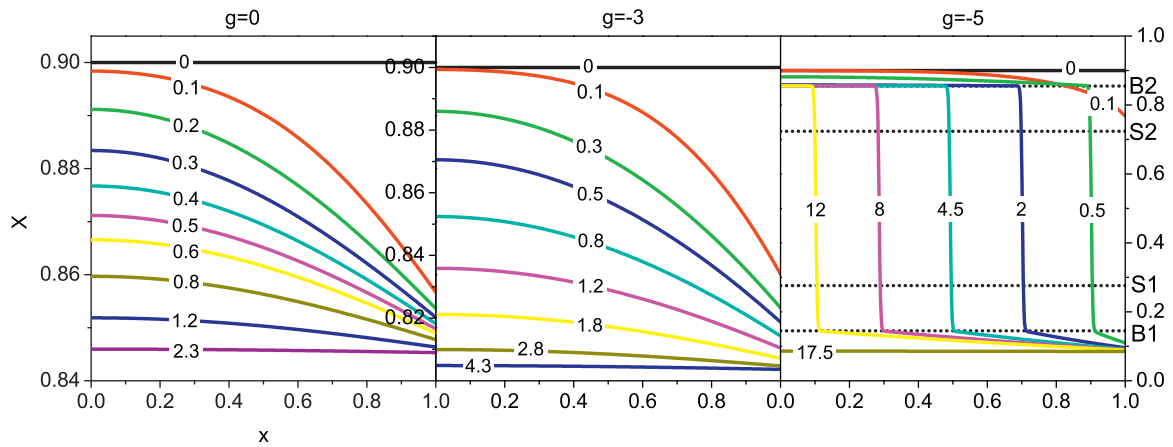
Fig. 8. Evolution of the concentration profile under a constant voltage step $\Delta v = 0.5$ and an interfacial resistance $R = 1$ for three different thermodynamic parameters $g = 0$, $g = -3$, and $g = -5$. Dimensionless times are shown on each curve. B1, B2, S1, and S2 points are the binodal and spinodal points discussed in Section 2.2. Particle surface and center are at the position of 1 and 0, respectively.

Laplace-inverse Laplace transform [12,30] as follows:

$$j(1)\sqrt{\tau} = \frac{X_0(1 - X_0)}{\sqrt{\pi \tilde{D}(X_0)}} \Delta \psi(1), \tag{65}$$

$$j(1) = 2X_0(1 - X_0)\exp\left[-\frac{\pi^2}{4}\tilde{D}(X_0)\tau\right]\Delta\psi(1), \tag{66}$$

where $\Delta\psi(1)$ is the voltage step. A slightly different form of Eq. (66) was also presented in Ref. [12] using a different series expansion.

Eq. (65) suggests that the product of current and the square root of time is a constant, also known as the Cottrell equation [14]. Eq. (66) suggests that the logarithm of current changes linearly with τ at long time periods. These are essentially the same equations as in the PITT Ref. [18].

The numerical simulation in this work involved the solid|liquid interface and made no assumption of small signals. Under these circumstances, the analytical solutions were not available. However, the results of the solid solutions are still presented in the form of
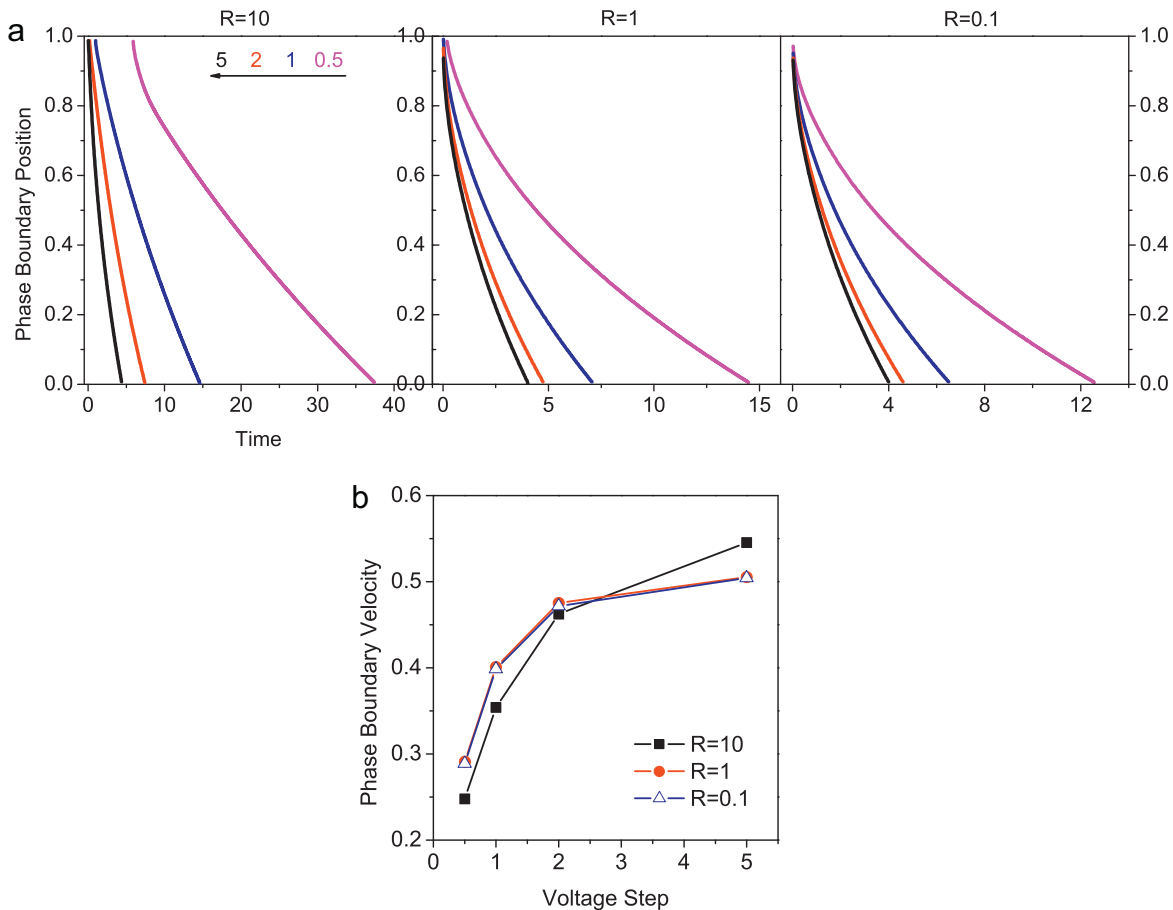

Fig. 9. (a) Phase boundary positions, and (b) phase boundary velocity constant under different values of voltage steps Δv (0.5, 1, 2, and 5) and interfacial resistances R for the phase transformation material with $g = -5$.

Eqs. (65) and (66) for comparison as dashed lines in Fig. 10(a)–(d), while the regular current vs. time plot is displayed in Fig. 10(e) for the phase transformation material.

For the short-time response of the solid solutions, Fig. 10(a) for $g = 0$ and Fig. 10(b) for $g = -3$, the Cottrell behavior can only be observed at small $R = 0.1$ values and small voltage step of $\Delta v = 0.2$. A small value of R suggested that it was under diffusion control, and a small voltage step Δv implied a small-signal perturbation. These two conditions led to results that were similar to those in Eqs. (65) and (66). As R became larger, i.e. toward to interface control, or Δv became larger, i.e. large signal, peak shaped plots were observed in Fig. 10(a) and (b). These types of peak shapes

have been observed experimentally for graphite [65] and LiFePO$_4$ [66].

For the long-time response of solid solutions, Fig. 10(c) for $g = 0$ and Fig. 10(d) for $g = -3$, a linear behavior can be observed in all the R and Δv values investigated. However, the slope only corresponded to values predicted from Eq. (66) in situations where approximations of diffusion control and small-signal can be satisfied, such as low R and Δv values. In the case of $g = -3$, Fig. 10(d), deviations of predicted slopes can be observed for most values studied.

For the case of phase transformation with $g = -5$, the current response following the voltage step, Fig. 10(e), exhibited some
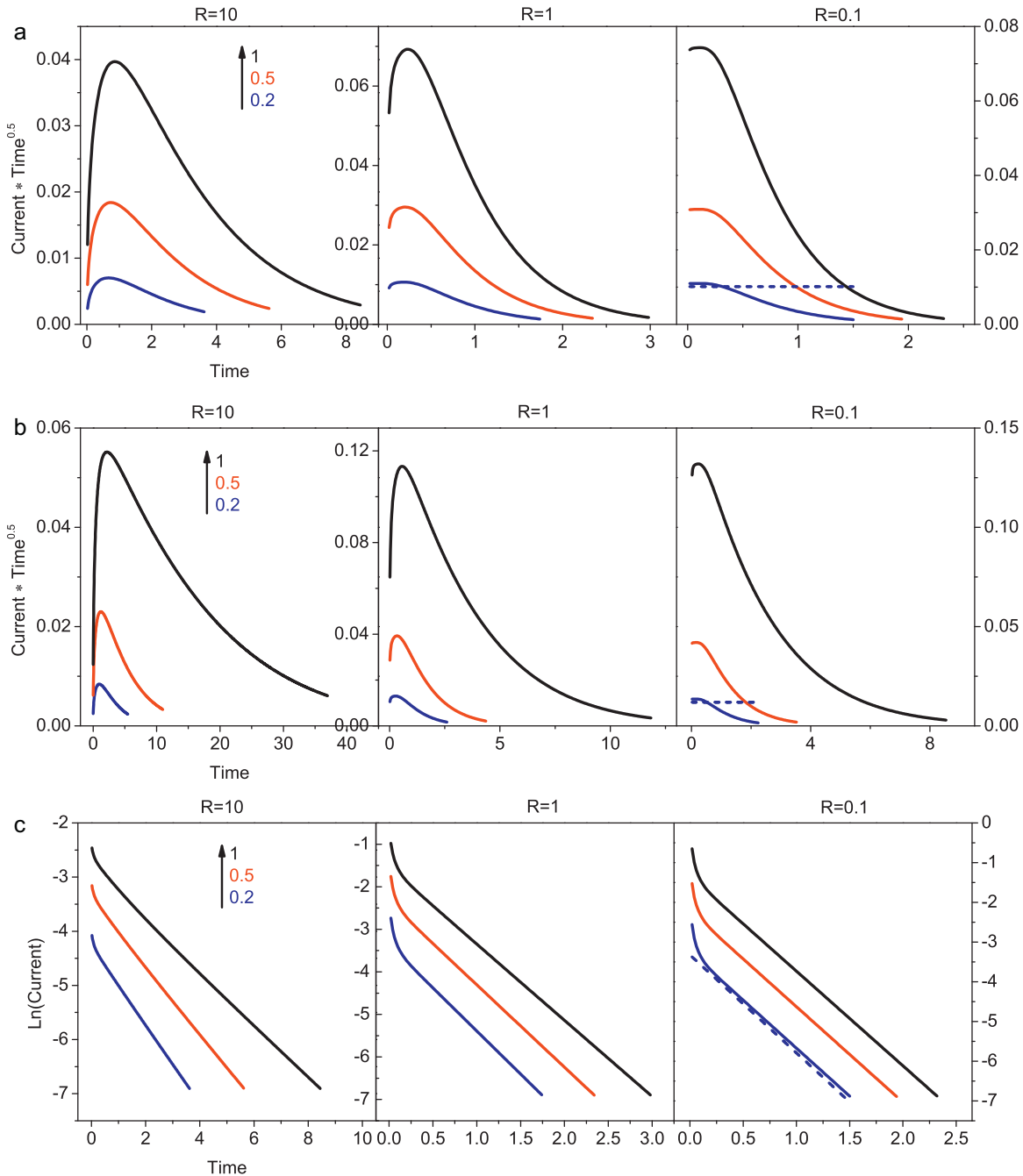

Fig. 10. Short-time characteristic curves according to Eq. (65) for (a) $g = 0$ and (b) $g = -3$ under three different voltage steps Δv (0.2, 0.5, and 1) and interfacial resistance R values. Dashed lines represent the expected plateau from small-signal assumption. Long-time characteristic curves according to Eq. (66) for (c) $g = 0$ and (d) $g = -3$ under three different voltage step and interfacial resistance values. Dashed lines represent the expected straight lines from small-signal assumption. (e) Current response for phase transformation material $g = -5$ under three different voltage step and interfacial resistance values.
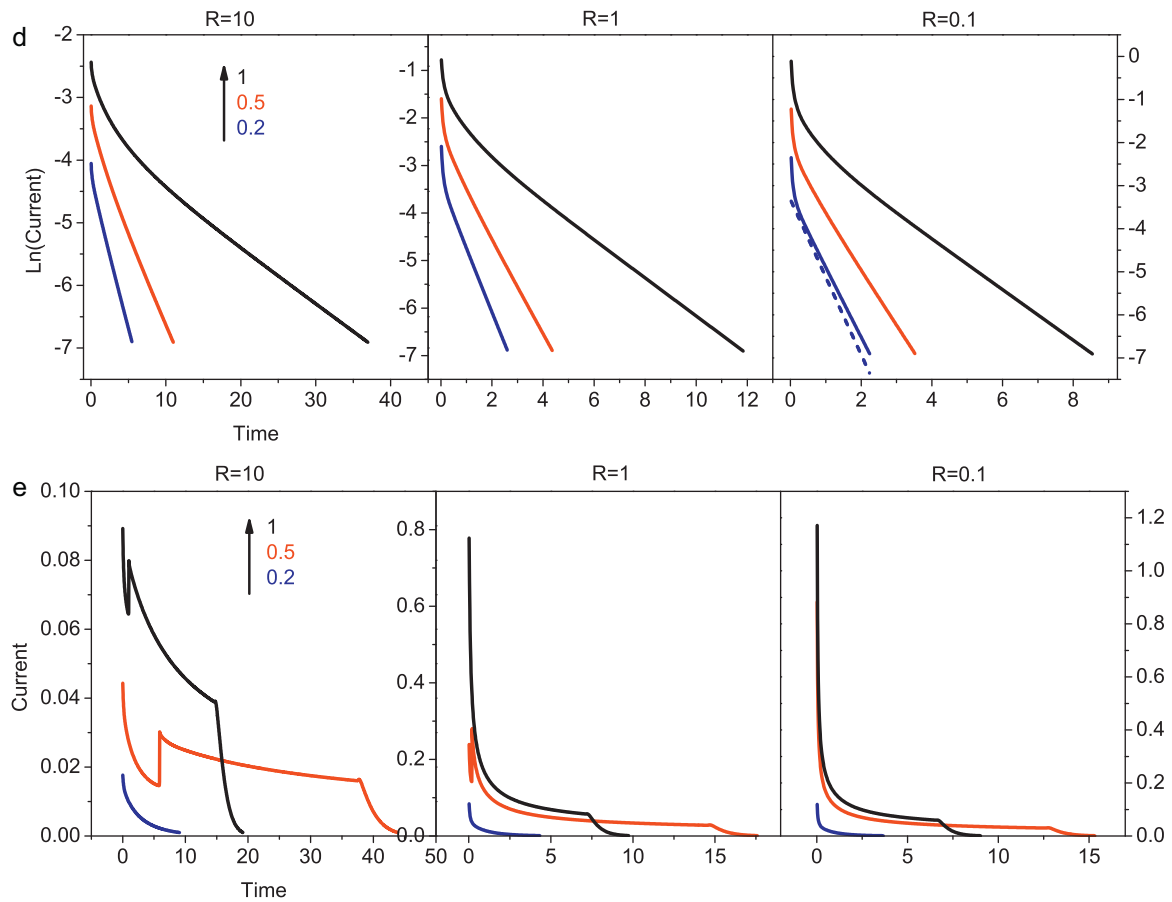
Fig. 10. (*Continued*).

interesting behavior. Initially, the material was in the single-phase region. When the voltage step Δv was small, e.g. 0.2, the material stayed as a single phase for all three R values, thus, the current decayed in a manner similar to Eqs. (65) and (66). As Δv increased to 0.5, the current spike was observed for R values of 10 and 1. The comparison of the current response in Fig. 10(e) and concentration evolution in Fig. 8 for the same set of data ($\Delta v = 0.5$ and $R = 1$) suggested that the current spike corresponded to the initiation of phase separation, and the kink at approximately $\tau = 15$ marked the finish of the separation. This behavior was observed more clearly with values of $\Delta v = 0.5$ and $R = 10$, which showed the initial single-phase decay, initiation of phase transformation, two-phase decay, and finally, another single-phase decay. The two separate single-phase decaying stages were similar to those of solid solutions with exponential decay, Fig. 10(c) and (d). The two-phase decay corresponded to the phase boundary movement, which appeared to be slower. As Δv increased further to 1 ($R = 1$), the initial spike disappeared, but the kink was still visible. This situation still progressed through the phase transformation cycle as in the case of $\Delta v = 0.5$. Physically, the initiation of phase separation and the phase boundary movement corresponded to nucleation and growth of the new phase.

First, the initial current increase upon voltage step was observed experimentally for graphite [67,68] and LiFePO$_4$ [66], though in the form of a hump instead of a spike. The hump was explained by the nucleation of new phases [66–68] and was quantitatively modeled by the Johnson–Mehl–Avrami equation [49,69]. Because the current spike in Fig. 10(e) was associated with the initiation of phase separation, it was expected that a homogenized model of many particles with a distribution of particle sizes and shapes would lead to a dispersion of time constants to form the hump observed in

those experimental composite electrodes. Second, the multi-staged current decay was also obtained from the sharp-interface moving boundary problem [58] and has been experimentally observed for Li$_4$Ti$_5$O$_{12}$ and Li$_\delta$V$_2$O$_5$ [70]. Finally, the square root dependence of the phase boundary movement was also related to the diffusion-controlled growth in the Johnson–Mehl–Avrami equation [49,69] and was also observed in in situ measurements of a single SnO$_2$ nanowire [71].

3.3. Linear sweep voltammetry

In linear sweep voltammetry, a linear scanning voltage $\Delta v = v^{LSV} \tau$ was applied and the current $j(1)$ was monitored as a function of time. The boundary condition used in Eq. (48) was transformed to the following:

$$j(1) = \frac{\psi(1, \tau = 0) - \psi(1) + v^{LSV} \tau}{R}. \tag{67}$$

Initially, the concentration X_0 was a uniform value of 0.99 in the solid, and the simulation was performed in the charging process. The scanning rates v^{LSV} were 0.05, 0.1, 0.2, 0.5, and 1. Time was incremented in steps of 0.02 till $X(1)$ fell below 0.01.

Current $j(1)$ is shown as a function of voltage $\psi(1, \tau = 0) + v^{LSV} \tau$ in Fig. 11 in voltammetry plot. Typical broad peaks were observed in the solid solutions, Fig. 11(a) for $g = 0$ and Fig. 11(b) for $g = -3$. The peak position for slow rates was at approximately zero voltage, and it moved to a higher voltage at faster scanning rates. The peak current also increased correspondingly. The difference between $R = 1$ and $R = 0.1$ was small, which suggested that they were close to the reversible (purely diffusion-controlled) mechanism.

The voltammetry plot of the phase transformation material $g = -5$ is shown in Fig. 11(c). For large $R = 10$, interface control, the plot was similar to those of solid solutions. Sudden current change was observed because of the initiation and termination of the phase transformation. For small $R = 0.1$, diffusion control, a sharp current peak was observed. Under pure diffusion control, a small variation of voltage caused a large current change because the voltage was flat for the phase transformation material. For the intermediate $R = 1$ value, a two-step current decay was observed at low scanning rates. Experimental voltammetry plots of battery materials, such as for LiCoO$_2$ [28,72,73], LiMn$_2$O$_4$ [72], graphite [74], and LiFePO$_4$ [75,76] generally have peak shapes similar to those of solid solutions in Fig. 11(a) and (b). However, they are different from those of phase transformation material in Fig. 11(c), although peak positions in those experimental plots correspond to the two-phase coexistence region in these materials. The simulation results in Fig. 11(c) represent only a single particle, and the dispersion of time constants in a composite electrode could broaden the peaks in Fig. 11(c).

Finally, the scanning rate dependence of the peak current data for all three thermodynamics is shown in Fig. 11(d). In classical liquid electrochemistry, the peak current of a redox reaction is proportional to the square root of scanning rate $\sqrt{v^{LSV}}$, known as Randles–Sevcik equation [15,22]. This was derived under the condition of the reversible reaction of an oxidant and reductant, semi-infinite diffusion, and constant concentration at infinity. In
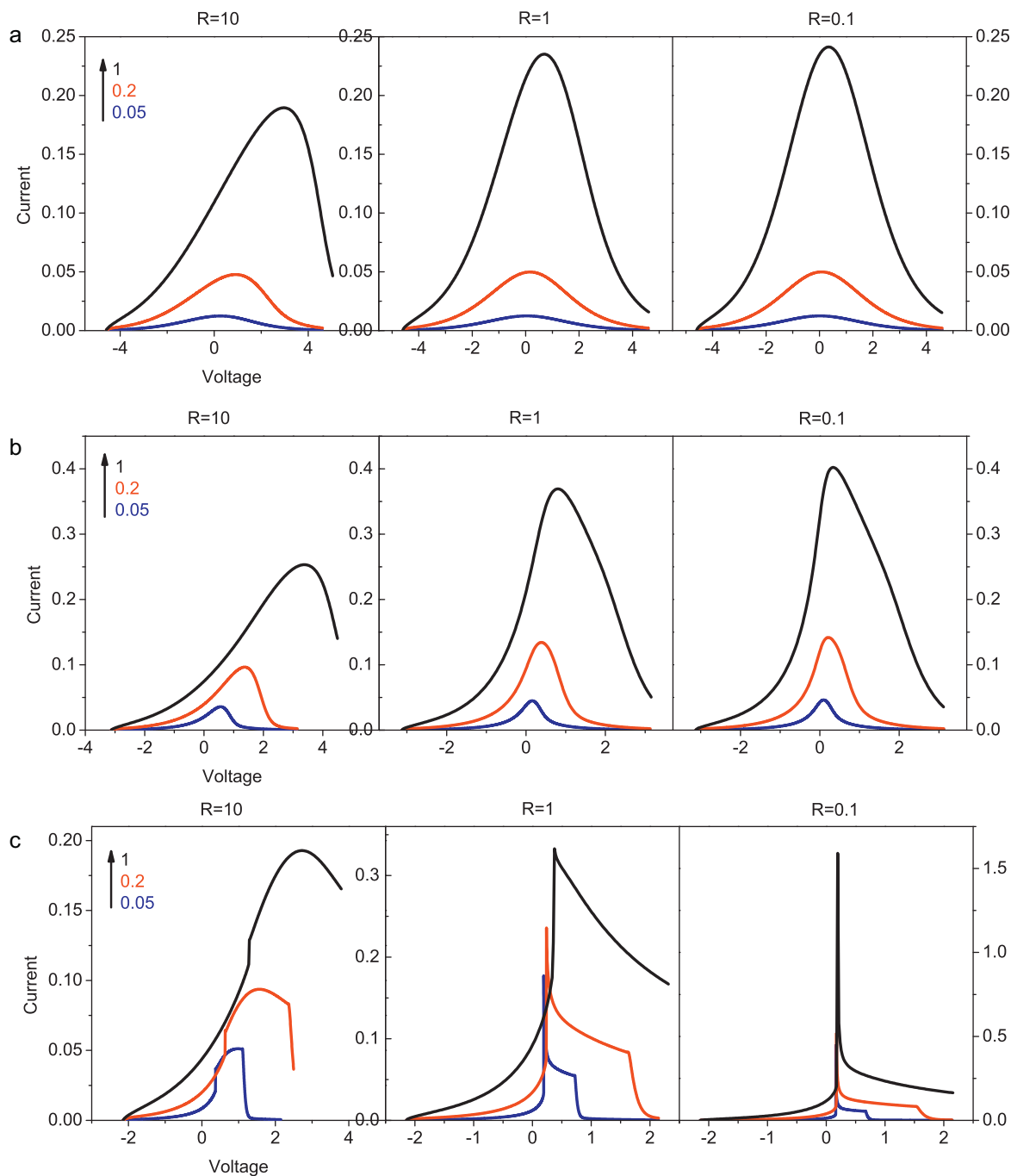

Fig. 11. Linear sweep voltammetry curves under three different rates v^{LSV} (0.05, 0.2, and 1) and interfacial resistances R of three different thermodynamics (a) $g = 0$, (b) $g = -3$, and (c) $g = -5$. (d) Peak current as a function of scanning rate for $g = 0$ and square root of scanning rate for $g = -3$, -5.
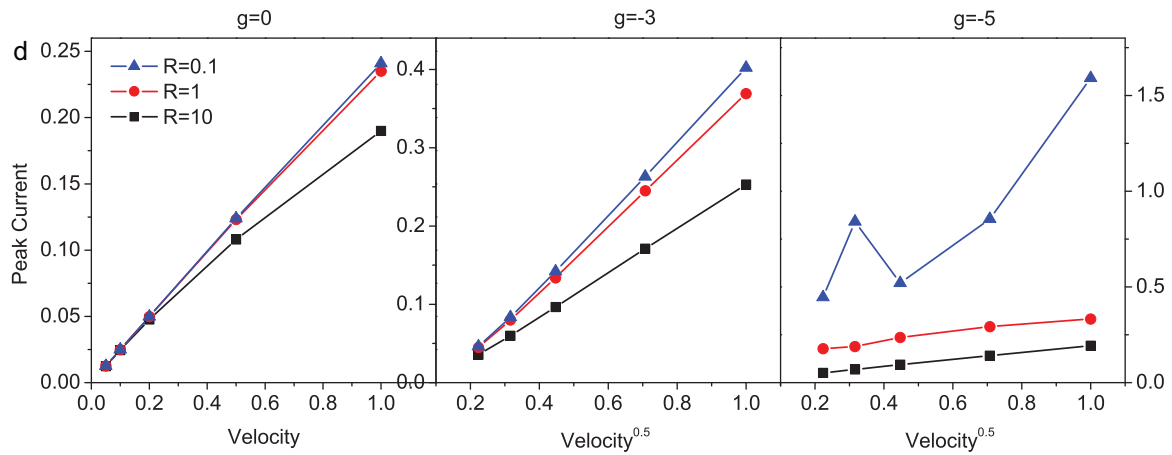
Fig. 11. (*Continued*).

the present work, the peak current was approximately proportional to v^{LSV} when $g = 0$ and it was roughly proportional to $\sqrt{v^{LSV}}$ when $g = -3, \ -5$. The clear exception was the case of reversible phase transformation ($R = 0.1$). The curves for $R = 1, \ 10$ were similar to those in the experimental investigation of LiFePO$_4$ [76]. In literatures, both the linear [75,77] and the square root dependence [78,79] on the scanning rate have been observed for LiFePO$_4$.

3.4. Impedance spectroscopy

In the simulation of impedance spectroscopy, a sinusoidal current $j(1)$ was applied and voltage response $\psi(1)$ was monitored. Similar to the constant-current case in Section 3.1, the additional interface contribution can be easily obtained. The boundary condition to be used in Eq. (48) became the following:

$$j(1) = j_{AC} \sin(\omega\tau) = j_{AC} \sin(2\pi f\tau), \tag{68}$$

where the dimensionless frequency was defined as follows:

$$f = f_{exp}t_0, \tag{69}$$

where f_{exp} is the experimental frequency in Hz.

Initially, the concentration X_0 was a uniform value of 0.9 in the solid. The amplitude of the sine wave j_{AC} was 0.0001, 0.001, 0.01, and 0.05. The dimensionless frequency f ranged from 0.05 to 1000. For each frequency, a digital sine wave with 1024 uniformly spaced points was applied for one period. Thus, the time stepping was 1/(1024f) until it reached 1/f. The translation of dimensionless frequency f to experimental frequency f_{exp} depended on t_0, as in Eq. (69). Thus, for a value of 1000 s of t_0, 0.05 of f translated to 0.05 mHz of f_{exp}, which was below the frequency that is normally applied in experiments. A value of 1000 for f translated to 1 Hz, which was low for the high frequency limit in real experiments. From the viewpoint of simulation, this dimensionless high frequency limit can be easily extended to above 1000, but simulation will require an increasing number of elements to insure convergence. For example, 5000 instead of 500 elements were required when a dimensionless frequency of 10^6 was used.

As for the cases of constant-current and constant-voltage signals in Sections 3.1 and 3.2, the evolution of concentration profiles was presented in Fig. 12 for a sine current wave with dimensionless amplitudes of 0.01 (left figure) and 0.05 (right figure) at a dimensionless frequency of 0.05, for the phase transformation material with $g = -5$. As expected, the oscillation of current at the particle surface $x = 1$ led to the oscillation of surface concentration. For the small amplitude of 0.01, phase separation was not initiated. For the larger amplitude of 0.05, the particle exhibited a two-phase coexistence at a quarter of a period with $\tau = 5$, and the phase boundary

oscillated from $\tau = 5$ to $\tau = 15$. The concentration at the end of the period was almost the same as the initial condition. The evolution of concentration profiles in the solid solutions was similar to values in the left figure of Fig. 12.

The solution of Eq. (48) with boundary conditions Eq. (68) provided the time domain voltage signal $\Delta\psi(1) = \psi(1) - \psi(1, \ \tau = 0)$, which can be expanded as a Fourier series [80]

$$\Delta\psi(1, \tau) = \frac{a_0}{2} + \sum_{n=1}^{\infty} A_n \cos(n\omega\tau + \phi_n), \tag{70}$$

where $a_0/2$ is the Faradaic rectification (DC component), A_n and ϕ_n are the amplitude and phase angle of the nth harmonic term. The classical impedance spectroscopy only looks at the 1st or fundamental harmonic term as in Eq. (61). These coefficients can be obtained from a Fast Fourier Transform based Fourier (harmonic) analysis detailed in Ref. [80].

Impedance spectra of the 1st harmonic in the form of a Nyquist plot are shown in Fig. 13(a) for the different amplitudes investigated, along with the analytical results (dashed lines) from Eq. (61) by replacing s with $i\omega$. The spectrum shape behaved as a series combination of a resistor and a capacitor at low frequencies and has been traditionally called the Warburg element with impermeable [30], reflecting [81], reflective [82], open [81], and restricted [83] boundary conditions, as well as a finite-space Warburg element [84] or T element [85]. Numerical results of the smallest amplitude of 0.0001 were closely matched to analytical results as expected. As the amplitude increased, deviations can be observed for both solid solutions and phase transformation material. This nonlinear behavior was due to the nonlinear form of the partial differential equations Eq. (48), common to all three cases. As g changed from 0 to -3 and -5, the diffusivity of Eq. (60) decreased, and vertical tail height decreased at the same frequency range. The nonlinear behavior can also be quantified from the harmonic analysis; the results are shown in Fig. 13(c). The voltage amplitude ratios of the 0th and 2nd harmonic term to the 1st harmonic term are plotted. First, the contribution of the 0th harmonic term (DC component) was always relatively large but this information is rarely studied theoretically or experimentally. Second, the 2nd harmonic term at the high frequency range increased slightly with increasing amplitude. In addition, even at the smallest amplitude of 0.0001, this contribution was close to 10%, and a slight deviation from analytical results (dashed lines) can be clearly observed in Fig. 13(b), with $g = -5$ and amplitude 0.05 as an example. Third, the 2nd harmonic term at the low frequency range increased greatly with increasing amplitude which can also be observed by the clear deviation in Fig. 13(a). Finally, for the phase transformation material with
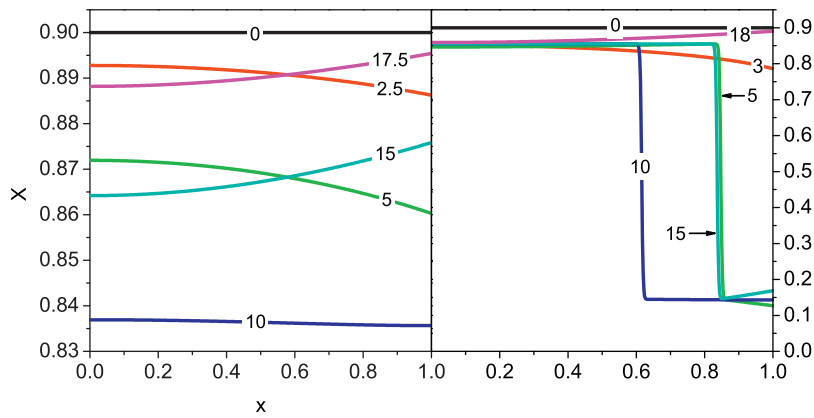
Fig. 12. Evolution of the concentration profile under a sinusoidal current of amplitude j_{AC} = 0.01 (left) and j_{AC} = 0.05 (right) for the phase transformation material with g = − 5. Dimensionless times are shown on each curve. The simulation was performed for one period of time 20. The curves corresponding to time 20 are almost the same as that at time 0 in both figures. Particle surface and center are at the position of 1 and 0, respectively.

g = − 5, a large sine current of 0.05 reached the unstable region and initiated the phase separation at low frequencies. This led to the largest deviation from the analytical results, which can be seen in Fig. 13(b).

3.5. Initial condition of "X = 0.5"

In addition to the initial concentrations of 0.9 and 0.99 discussed above, a value of 0.5 seemed to be another interesting initial con-

centration. However, as can be seen in Fig. 2(a), this concentration corresponds to a separation of two phases for the phase transformation material with g = − 5. In other words, a uniform concentration profile of 0.5 is not a valid initial condition for g = − 5.

Instead, the particle was charged at a constant current of 0.1 for the duration of dimensionless time of 4, starting from a uniform concentration of 0.9. The delivered capacity will change the overall average concentration to 0.5. Then the current was turned off and the particle was relaxed for another time period of 4. For solid solu-
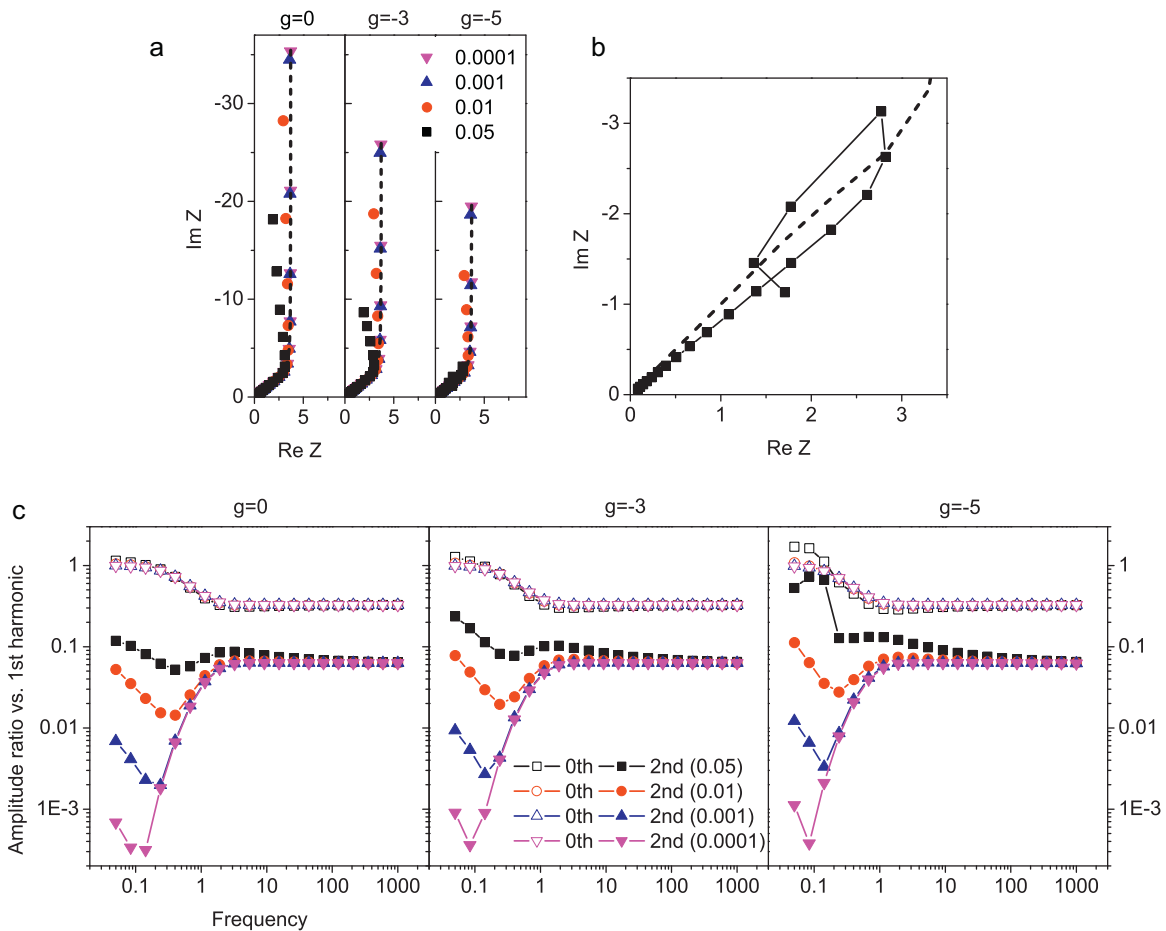

Fig. 13. (a) Nyquist plot of the 1st order harmonic term under different current amplitudes j_{AC} (0.0001, 0.001, 0.01, and 0.05) for three thermodynamic parameters g = 0, (b) g = − 3, and (c) g = − 5. (b) Enlarged Nyquist plot at high frequencies under an amplitude of 0.05 for g = − 5. (c) Voltage amplitude ratios of the 0th and 2nd order harmonic terms to that of the 1st order harmonic term at different current amplitudes and frequencies.
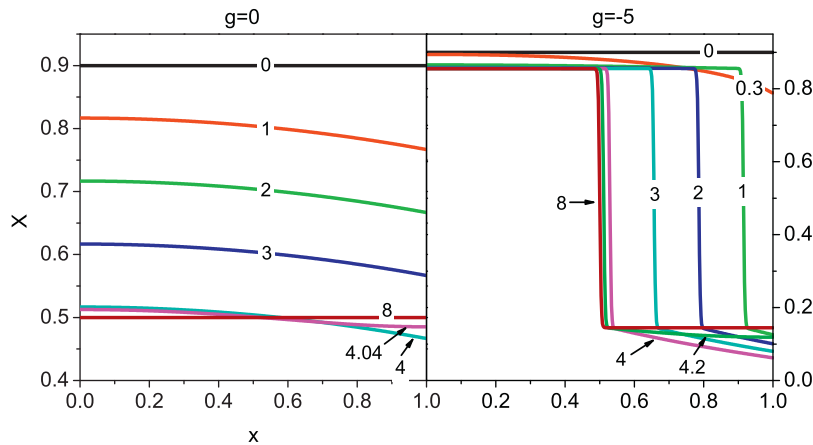
Fig. 14. Evolution of concentration profile of a solid solution $g=0$ (left) and a phase transformation material $g=-5$ (right), under a constant current $j(1)=0.1$ for a time of 4 followed by relaxation for a time of 4. Dimensionless times are shown on each curve. Particle surface and center are at the position of 1 and 0, respectively.

tions, the concentration profile was expected to relax to a uniform value of 0.5 across the particle. The case of $g=0$ is shown in the left figure of Fig. 14 with labeled dimensionless times. Similar behavior was found for the case of $g=-3$. However, for $g=-5$ (right figure), the final relaxed state of apparent concentration of 0.5 exhibited the coexistence of two phases. The two phases had the same compositions of binodal points B1 and B2 in Fig. 2(a). These two different behaviors can be understood by Eq. (48). A zero current during relaxation implied a constant value of ψ across the particle. For solid solutions, $\gamma = 0$ led to constant values of concentration everywhere. Conversely, a concentration gradient was possible with a nonzero value of γ. A good analog was the space charge concept with the balance of concentration and electrical driving forces [86].

3.5.1. GITT

In the context of GITT, the right-hand side of Eq. (63) is a constant. This condition was not satisfied for an initial uniform concentration of 0.99 shown in Fig. 7. The same types of plots are shown in Fig. 15 for solid solutions with a uniform concentration of 0.5 and phase transformation material with initial two-phase coexistence. The dashed lines are the calculated results from Eq. (63). A plateau was obtained up to an approximate time of 0.5 for $g=0$ and 1 for $g=-3$. The data with $g=-5$ were close to constant and oscillated around the dashed line.

The difference between Figs. 7 and 15 can be understood by the assumption used to obtain Eq. (63), i.e. the application of current

step leading to a small value of $\Delta\psi$. For the initial concentration of 0.99, the equilibrium curve was steeper compared to those of the initial concentration of 0.5, Fig. 2(a). Thus, it was more difficult to meet the small-signal approximation for concentration of 0.99.

3.5.2. PITT

For the initial concentration profile in Fig. 14 of the phase transformation material, current decay following the voltage step is shown in Fig. 16. Compared to the initial condition with a single-phase, Fig. 10(e), the first stage single-phase decay and current spike disappeared because the particle was initially at the two-phase coexistence.

3.5.3. EIS

For solid solutions with $g=0$, -3, simulation results for the initial uniform concentration of 0.5 (Fig. 17(a)), exhibited similar shapes compared to those for the concentration of 0.9, Fig. 13(a). Again, dashed lines represented results predicted from the analytical expression of Eq. (61). Impedance spectra appeared linear up to an amplitude of 0.01. At higher amplitude, e.g. 0.05, impedance values became larger as opposed to smaller in Fig. 13(a). Harmonic analysis, Fig. 17(b), revealed similar DC and 2nd harmonic terms compared to those in Fig. 13(c).

However, in Fig. 17(a), the impedance spectra of the phase transformation material $g=-5$ have different shapes from those for the concentration of 0.9, Fig. 13(a). This shape behaved as a
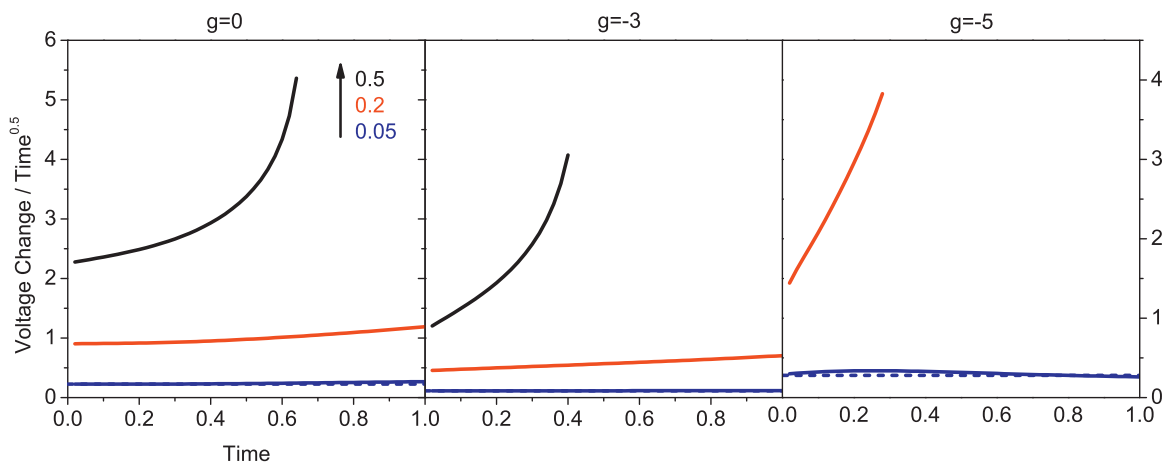

Fig. 15. Short-time characteristic curves according to Eq. (63) under three different currents for three different thermodynamic parameters $g=0$, $g=-3$, and $g=-5$. Dashed lines represent the plateaus expected from the small-signal assumption. The initial condition is the relaxed state in Fig. 14, i.e. "$X=0.5$".
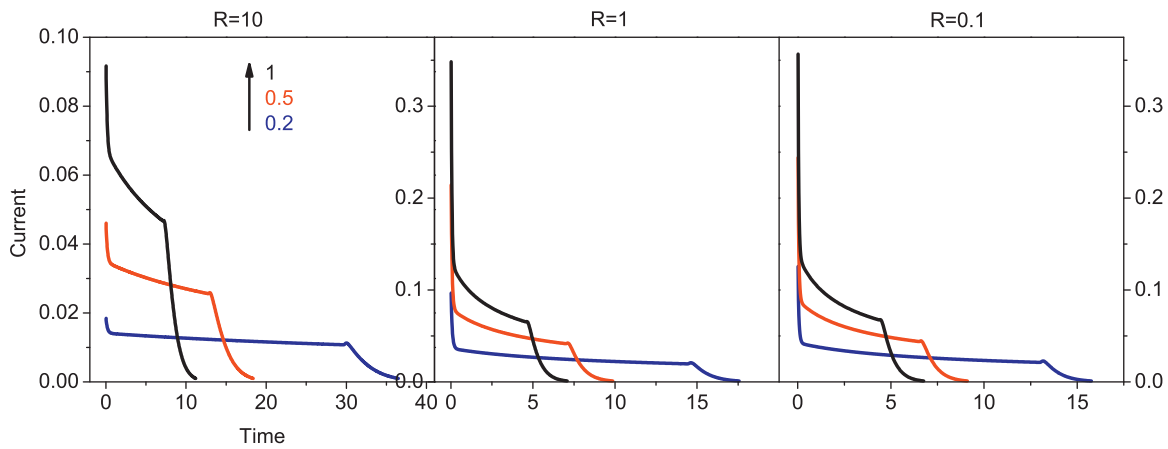
Fig. 16. Current response for phase transformation material with $g = -5$ under three different voltage step and interfacial resistance values. The initial condition is the relaxed state in Fig. 14, i.e. "$X = 0.5$".

resistor instead of a capacitor at low frequencies and has been traditionally called the Warburg element with Nernstian [30], absorbing [81], transmissive [82], short [81], and bounded [83] boundary conditions, and finite-length Warburg element [84] or O element [85]. The dashed line corresponds to a reflective Warburg element predicted according to Eq. (61) from a uniform initial concentration of the binodal point B1. The outer half of the particle had this concentration of B1 as can be seen in Fig. 14. Similar experimental impedance spectra compared to those in Fig. 17(a) were observed for the 50% charged LiFePO₄ electrode [87].

The analytical result that led to the reflective Warburg element was obtained under the assumption of a constant initial concentration and a small-signal perturbation. Thus, it was natural to compare concentration profiles obtained from the current initial condition and those from the uniform initial concentration of 0.9. Fig. 18 shows the concentration evolution under a sine wave of amplitudes 0.01 (left) and 0.05 (right) at a frequency of 0.05. The initial condition $\tau = 0$ was the relaxed state in Fig. 14. It was apparent that neither of the figures in Fig. 18 satisfied the constant initial concentration condition, although the signal on the left figure can be considered small amplitude. Oscillation of surface concentration
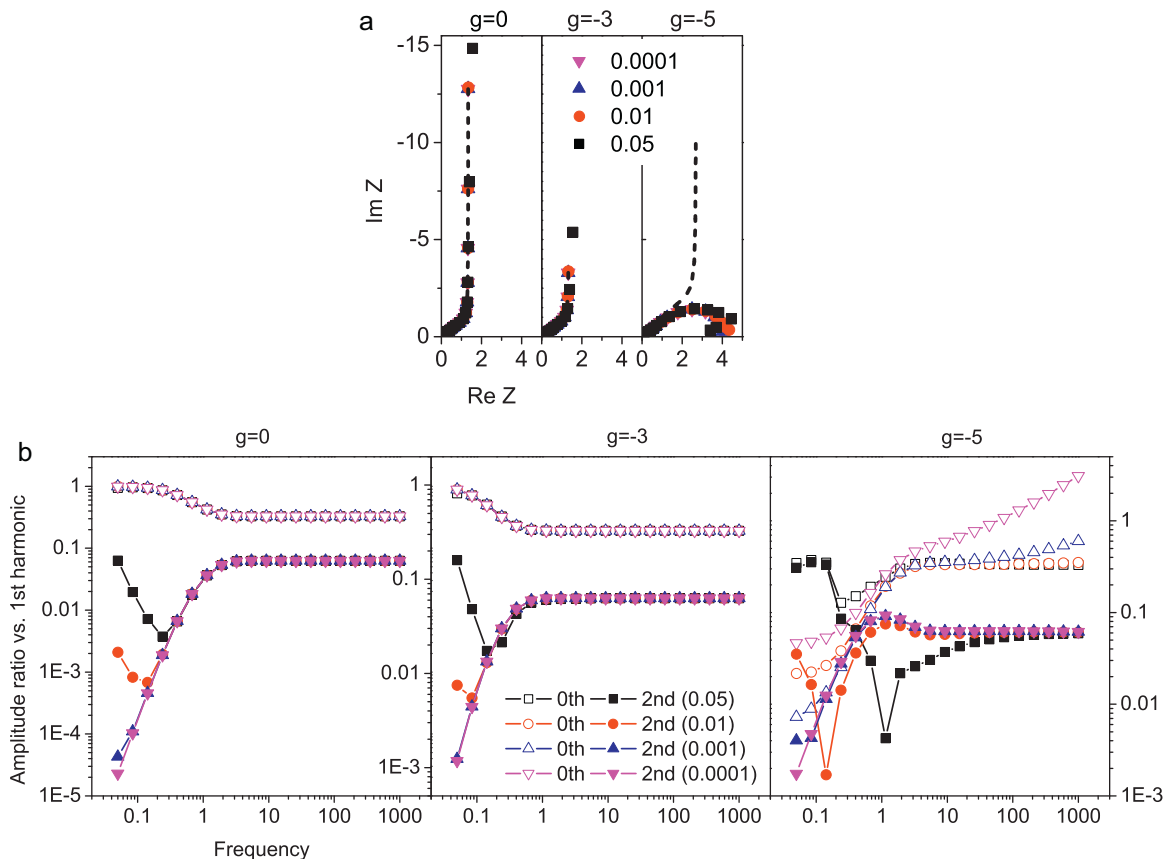

Fig. 17. (a) Nyquist plot of the 1st order harmonic term under different current amplitudes for three thermodynamic parameters $g = 0$, (b) $g = -3$, and (c) $g = -5$. The initial condition is the relaxed state in Fig. 14, i.e. "$X = 0.5$". (b) Voltage amplitude ratios of the 0th and 2nd order harmonic terms to that of the 1st order harmonic term at different current amplitudes and different frequencies.
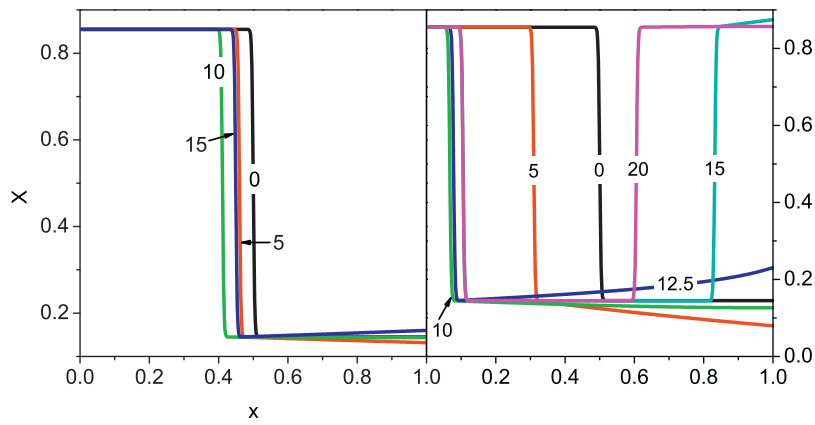
Fig. 18. Evolution of the concentration profile of a solid solution $g = 0$ and a phase transformation material $g = -5$, under sine waves of amplitudes 0.01 (left) and 0.05 (right) at a frequency of 0.05. The initial condition is the relaxed state in Fig. 14, i.e. "$X = 0.5$". Dimensionless times are shown on each curve. The simulation was performed for one period of time 20. The curve corresponding to time 20 is almost the same as that at time 0 for the left figure. Particle surface and center are at the position of 1 and 0, respectively.

was accompanied by the "in-phase" oscillation of phase boundary, and this was the reason that a transmissive Warburg element was observed in Fig. 17(a) ($g = -5$). Harmonic analysis of Fig. 17(b) reveals larger harmonic terms with higher input amplitudes at low frequencies. Finally, it was interesting to note that a large sine current could induce a peculiar phase I|II|I sandwich structure, e.g. between time 15 and 20 on the right figure of Fig. 18. It is possible that this structure can also be obtained by applying any large amplitude *discharging* signal from the initial condition in Fig. 14, although this has been rarely discussed theoretically or experimentally.

3.6. Symmetry effect

All the above numerical results were obtained for the planar symmetry $m = 0$ to facilitate a comparison with the well-known relations such as the Cottrell, Randles–Sevcik equation, etc. Small-signal solutions with short-time and long-time approximations have been determined for spherical, cylindrical, and planar symmetry, under the application of a constant-current, constant-voltage, and sinusoidal current/voltage in Ref. [12]. The numerical simulation with arbitrary magnitude signal suggested that many features shown in previous sections were common to all three symmetries (not shown). One difference worth pointing out was that the two-stage current-decaying behavior found for the constant-voltage and linear sweep voltage signals (Figs. 10(e) and 11(c)), was less distinct for the cylindrical and spherical symmetry. Current wave-

forms for the voltage step with $R = 10$ and the linear sweep voltage with $R = 1$ are shown in Fig. 19. In both figures, the distinction of current decay due to phase boundary movement and the following single-phase diffusion was subtler for spherical symmetry compared to planar symmetry. Another difference was the time dependence of the phase boundary position in different symmetries. The phase boundary position to the second (spherical), one and half (cylindrical), and first (planar) power had a square root and linear time dependence under the voltage and current step, respectively.

3.7. Applicability of present work to real battery materials

This simulation study provided herein presents a framework that employs a regular solution model (thermodynamic) and a generalized Poisson–Nernst–Planck equation set with a resistive boundary condition (kinetic) on a single particle (microstructure). The parameter space was $[c_+^0, r_0, \mu_+^0, g, \gamma, D_+^0, R]$. Variables c_+^0 and r_0 were the maximum concentration and particle size along the symmetry direction, respectively. Variables μ_+^0 and g were related to the voltage plateau and miscibility gap [47] of the voltage curve. Variable γ represented the interfacial energy between coexisting solid phases during the phase transformation. Diffusivity D_+^0 was the primary kinetic parameter which was also related to the ionic conductivity or mobility through Eqs. (27) and (28). Finally, R represented the resistance across the solid|liquid interface.
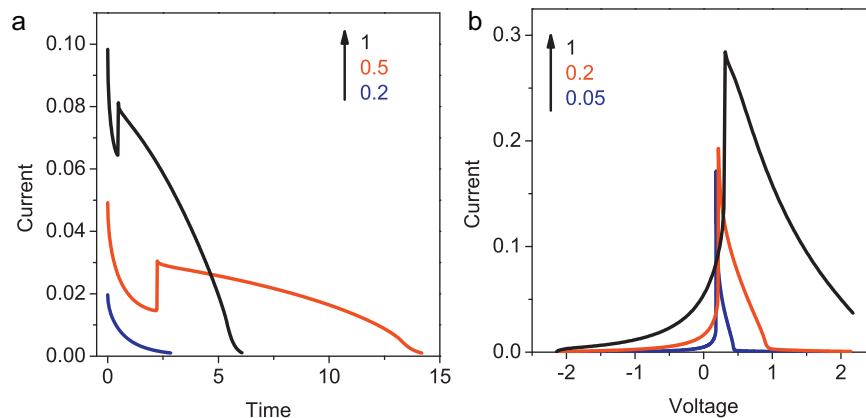

Fig. 19. (a) Current response for the spherical phase transformation material with $g = -5$ under three different voltage steps Δv (0.2, 0.5, and 1) and $R = 10$. The initial condition is a uniform concentration of 0.9. (b) Linear sweep voltammetry curves for spherical phase transformation material $g = -5$ under three different rates v^{LSV} (0.05, 0.2, and 1) and $R = 1$. The initial condition is a uniform concentration of 0.99.

One or more components of the thermodynamics, kinetics, and microstructure may have to be improved to allow more quantitative comparison with experimental data, usually from composite electrodes. For example, the regular solution model can only roughly approximate the phase transformation materials such as Li_xFePO_4 [63,88] and $Li_{4+3x}Ti_5O_{12}$ [89], with pseudo anti-symmetrical voltage curves. In the previous phase field study of Li_xFePO_4, g values of -4.7 [39] and -10 [38,48] were used. The interfacial energy between coexisting phase is normally difficult to measure experimentally, and estimates of values related to interfacial energy parameter γ were also provided in references for Li_xFePO_4 [38,39,48]. On the other hand, the regular solution model generally cannot be applied to other common materials, such as Li_xCoO_2 [22], Li_xC_6 [90,91], or $Li_xMn_2O_4$ [92,93], which have more complex voltage dependences. These materials have more than one two-phase coexistence regions. A discussion on the correlation of other thermodynamic models and properties with practical battery materials will appear in another manuscript.

The present simulation can easily be extended to more than one dimension by using the original equations with gradients and Laplacians, Eqs. (5)–(8). In addition, the single particle consideration can easily be extended to a collection of particles, where either pseudo 2D symmetry from volume averaging [13,51,52], or the brute-force 2D [94] or 3D [95] calculations can be performed.

4. Conclusions

Numerical modeling of a single intercalation battery particle was performed in this study for four different electrical signals, such as the current step, voltage step, linear sweep voltage, and the sinusoidal voltage. Techniques that utilize these signals are generally known as constant-current charging/GITT, constant-voltage charging/PITT, CV, and EIS in the battery field. Thermodynamic and kinetic properties of interest included a solid solution with constant diffusivity, a solid solution with variable diffusivity, and a phase transformation material. In addition, the interfacial behavior of particle and liquid electrolyte was incorporated as a resistor. It was found that the known small-signal solutions of GITT, PITT, and EIS were valid only under the conditions of a uniform initial concentration profile, a small-signal perturbation, and no interfacial effects. Some interesting phenomena were observed from the simulation of the phase transformation material. Typical progression for the current/voltage response in the phase transformation exhibited a single-phase diffusion, the initiation of phase separation, movement of the phase boundary, and another single-phase diffusion. This has important implications in the interpretation of experimental data involving phase transformation battery materials.

Acknowledgement

References

[1] R.P. Buck, J. Membr. Sci. 17 (1984) 1–62.
[2] M.Z. Bazant, K. Thornton, A. Ajdari, Phys. Rev. E 70 (2004) 021506.
[3] T. Grasser, T.W. Tang, H. Kosina, S. Selberherr, Proc. IEEE 91 (2003) 251–274.
[4] R.S. Eisenberg, J. Membr. Biol. 150 (1996) 1–25.
[5] J. Crank, The Mathematics of Diffusion, 2nd ed., Oxford University Press, New York, NY, 1980.
[6] T.R. Brumleve, R.P. Buck, J. Electroanal. Chem. 126 (1981) 73–104.
[7] R.P. Buck, C. Mundt, Electrochim. Acta 44 (1999) 1999–2018.
[8] J. Jamnik, J. Maier, Phys. Chem. Chem. Phys. 3 (2001) 1668–1678.
[9] W. Lai, S.M. Haile, J. Am. Ceram. Soc. 88 (2005) 2979–2997.
[10] W. Lai, S.M. Haile, Phys. Chem. Chem. Phys. 10 (2008) 865–883.
[11] W. Lai, F. Ciucci, Electrochim. Acta 56 (2010) 531–542.
[12] W. Lai, F. Ciucci, J. Electrochem. Soc. 158 (2011) A115–A121.
[13] W. Lai, F. Ciucci, Electrochim. Acta. doi:10.1016/j.electacta.2011.01.012.
[14] A.J. Bard, L.R. Faulkner, Electrochemical Methods: Fundamentals and Applications, 2nd ed., John Wiley & Sons Inc., New York, NY, 2000.
[15] A.J. Bard, G. Inzelt, F. Scholz (Eds.), Electrochemical Dictionary, Springer, Berlin, Germany, 2008.
[16] D. Linden, T.B. Reddy (Eds.), Handbook of Batteries, McGraw-Hill Companies Inc., New York, NY, 2001.
[17] W. Weppner, R.A. Huggins, J. Electrochem. Soc. 124 (1977) 1569–1578.
[18] C.J. Wen, B.A. Boukamp, R.A. Huggins, W. Weppner, J. Electrochem. Soc. 126 (1979) 2258–2266.
[19] E. Barsoukov, J.R. Macdonald (Eds.), Impedance Spectroscopy: Theory, Experiment, and Applications, John Wiley & Sons Inc., Hoboken, NJ, 2005.
[20] F. Kremer, A. Schonhals (Eds.), Broadband Dielectric Spectroscopy, Springer, Berlin, Germany, 2002.
[21] M.E. Orazem, B. Tribollet, Electrochemical Impedance Spectroscopy, John Wiley & Sons Inc., Hoboken, NJ, 2008.
[22] M.D. Levi, G. Salitra, B. Markovsky, H. Teller, D. Aurbach, U. Heider, L. Heider, J. Electrochem. Soc. 146 (1999) 1279–1289.
[23] S. Atlung, K. West, T. Jacobsen, J. Electrochem. Soc. 126 (1979) 1311–1321.
[24] E. Deiss, Electrochim. Acta 50 (2005) 2927–2932.
[25] V.R. Subramanian, J.A. Ritter, R.E. White, J. Electrochem. Soc. 148 (2001) E444–E449.
[26] C. Montella, J. Electroanal. Chem. 518 (2002) 61–83.
[27] E. Deiss, Electrochim. Acta 47 (2002) 4027–4034.
[28] H.C. Shin, S.I. Pyun, Electrochim. Acta 46 (2001) 2477–2485.
[29] C. Montella, J. Electroanal. Chem. 614 (2008) 121–130.
[30] T. Jacobsen, K. West, Electrochim. Acta 40 (1995) 255–262.
[31] S.R. De Groot, P. Mazur, Non-Equilibrium Thermodynamics, Dover Publications, Mineola, NY, 1984.
[32] F. Ciucci, W. Lai, Transport Porous Media. doi:10.1007/s11242-011-r9738-5.
[33] P. Atkins, J. De Paula, Physical Chemistry, Oxford University Press, Oxford, UK, 2006.
[34] S. Stolen, T. Grande, N.L. Allan, Chemical Thermodynamics of Materials, John Wiley & Sons, West Sussex, UK, 2004.
[35] W.R. McKinnon, R.R. Haering, in: R.E. White, J.O.M. Bockris, B.E. Conway (Eds.), Modern Aspects of Electrochemistry, vol. 15, Plenum Press, New York, NY, 1983, pp. 235–304.
[36] S.T. Coleman, W.R. McKinnon, J.R. Dahn, Phys. Rev. B 29 (1984) 4147–4149.
[37] M.D. Levi, D. Aurbach, Electrochim. Acta 45 (1999) 167–185.
[38] G.K. Singh, G. Ceder, M.Z. Bazant, Electrochim. Acta 53 (2008) 7599–7613.
[39] B.C. Han, A. Van der Ven, D. Morgan, G. Ceder, Electrochim. Acta 49 (2004) 4691–4699.
[40] H.B. Callen, Thermodynamics and an Introduction to Thermostatistics, John Wiley & Sons, 1985.
[41] K. Thornton, J. Agren, P.W. Voorhees, Acta Mater. 51 (2003) 5675–5710.
[42] L.Q. Chen, Ann. Rev. Mater. Res. 32 (2002) 113–140.
[43] M. Tang, W.C. Carter, R.M. Cannon, Phys. Rev. B 73 (2006) 024102.
[44] W.J. Boettinger, J.A. Warren, C. Beckermann, A. Karma, Ann. Rev. Mater. Res. 32 (2002) 163–194.
[45] J.E. Guyer, W.J. Boettinger, J.A. Warren, G.B. McFadden, Phys. Rev. E 69 (2004) 021603.
[46] J.E. Guyer, W.J. Boettinger, J.A. Warren, G.B. McFadden, Phys. Rev. E 69 (2004) 021604.
[47] D. Burch, M.Z. Bazant, Nano Lett. 9 (2009) 3795–3800.
[48] M. Tang, H.Y. Huang, N. Meethong, Y.H. Kao, W.C. Carter, Y.M. Chiang, Chem. Mater. 21 (2009) 1557–1571.
[49] M. Tang, W.C. Carter, Y.M. Chiang, Ann. Rev. Mater. Res. 40 (2010) 501–529.
[50] J.W. Cahn, J.E. Hilliard, J. Chem. Phys. 28 (1958) 258–267.
[51] M. Doyle, T.F. Fuller, J. Newman, J. Electrochem. Soc. 140 (1993) 1526–1533.
[52] T.F. Fuller, M. Doyle, J. Newman, J. Electrochem. Soc. 141 (1994) 1–10.
[53] J. Newman, K.E. Thomas-Alyea, Electrochemical Systems, John Wiley & Sons Inc., Hoboken, NJ, 2004.
[54] I. Riess, J. Maier, J. Electrochem. Soc. 156 (2009) P7–P20.
[55] H.C. Chang, G. Jaffe, J. Chem. Phys. 20 (1952) 1071–1077.
[56] A.V. Virkar, J. Power Sources 147 (2005) 8–31.
[57] A.V. Virkar, J. Power Sources 194 (2009) 753–762.
[58] H.C. Shin, S.I. Pyun, Electrochim. Acta 45 (1999) 489–501.
[59] COMSOL Multiphysics, 1998–2011 COMSOL AB.
[60] J. Molenda, A. Stoklosa, T. Bak, Solid State Ionics 36 (1989) 53–58.
[61] W. Lai, C.K. Erdonmez, T.F. Marinis, C.K. Bjune, N.J. Dudney, F. Xu, R. Wartena, Y.M. Chiang, Adv. Mater. 22 (2010) E139–E144.
[62] Z.H. Chen, J.R. Dahn, Electrochim. Acta 49 (2004) 1079–1090.
[63] N. Meethong, H.Y.S. Huang, W.C. Carter, Y.M. Chiang, Electrochem. Solid-State Lett. 10 (2007) A134–A138.
[64] R.W. Balluffi, S.M. Allen, W.C. Carter, Kinetics of Materials, John Wiley and Sons, Hoboken, NJ, 2005, pp. 501–531.
[65] D. Aurbach, M.D. Levi, E. Levi, Solid State Ionics 179 (2008) 742–751.
[66] N. Meethong, Y.H. Kao, W.C. Carter, Y.M. Chiang, Chem. Mater. 22 (2010) 1088–1097.
[67] A. Funabiki, M. Inaba, T. Abe, Z. Ogumi, J. Electrochem. Soc. 146 (1999) 2443–2448.
[68] M.D. Levi, E. Markevich, D. Aurbach, Electrochim. Acta 51 (2005) 98–110.
[69] J.L. Allen, T.R. Jow, J. Wolfenstine, Chem. Mater. 19 (2007) 2108–2111.
[70] H.C. Shin, S.I. Pyun, S.W. Kim, M.H. Lee, Electrochim. Acta 46 (2001) 897–906.

[71] J.Y. Huang, L. Zhong, C.M. Wang, J.P. Sullivan, W. Xu, L.Q. Zhang, S.X. Mao, N.S. Hudak, X.H. Liu, A. Subramanian, H.Y. Fan, L.A. Qi, A. Kushima, J. Li, Science 330 (2010) 1515–1520.
[72] D.A. Totir, B.D. Cahan, D.A. Scherson, Electrochim. Acta 45 (1999) 161–166.
[73] J. Barker, R. Pynenburg, R. Koksbang, M.Y. Saidi, Electrochim. Acta 41 (1996) 2481–2488.
[74] M.D. Levi, D. Aurbach, J. Electroanal. Chem. 421 (1997) 79–88.
[75] F. Sauvage, E. Baudrin, L. Gengembre, J.M. Tarascon, Solid State Ionics 176 (2005) 1869–1876.
[76] D.Y.W. Yu, C. Fietzek, W. Weydanz, K. Donoue, T. Inoue, H. Kurokawa, S. Fujitani, J. Electrochem. Soc. 154 (2007) A253–A257.
[77] S. Franger, C. Bourbon, F. Le Cras, J. Electrochem. Soc. 151 (2004) A1024–A1027.
[78] S.W. Song, R.P. Reade, R. Kostecki, K.A. Striebel, J. Electrochem. Soc. 153 (2006) A12–A19.
[79] M. Takahashi, S. Tobishima, K. Takei, Y. Sakurai, Solid State Ionics 148 (2002) 283–289.
[80] W. Lai, Electrochim. Acta 55 (2010) 5511–5518.
[81] J. Bisquert, J. Phys. Chem. B 106 (2002) 325–333.
[82] A. Lasia, in: B.E. Conway, J. Bockris, R.E. White (Eds.), Modern Aspects of Electrochemistry, vol. 32, Kluwer Academic/Plenum Publishers, New York, NY, 1999, pp. 143–248.
[83] J.P. Diard, B. Le Gorrec, C. Montella, J. Electroanal. Chem. 471 (1999) 126–131.
[84] M.D. Levi, C. Wang, D. Aurbach, J. Electroanal. Chem. 561 (2004) 1–11.
[85] V. Freger, S. Bason, J. Membr. Sci. 302 (2007) 1–9.
[86] S. Kim, J. Maier, J. Electrochem. Soc. 149 (2002) J73–J83.
[87] M. Gaberscek, R. Dominko, J. Jamnik, J. Power Sources 174 (2007) 944–948.
[88] A.K. Padhi, K.S. Nanjundaswamy, J.B. Goodenough, J. Electrochem. Soc. 144 (1997) 1188–1194.
[89] T. Ohzuku, A. Ueda, N. Yamamoto, J. Electrochem. Soc. 142 (1995) 1431–1435.
[90] J.R. Dahn, Phys. Rev. B 44 (1991) 9170–9177.
[91] T. Ohzuku, Y. Iwakoshi, K. Sawai, J. Electrochem. Soc. 140 (1993) 2490–2498.
[92] T. Ohzuku, M. Kitagawa, T. Hirai, J. Electrochem. Soc. 137 (1990) 769–775.
[93] M.M. Thackeray, Prog. Solid State Chem. 25 (1997) 1–71.
[94] M. Smith, R.E. Garcia, Q.C. Horn, J. Electrochem. Soc. 156 (2009) A896–A904.
[95] C.W. Wang, A.M. Sastry, J. Electrochem. Soc. 154 (2007) A1035–A1047.